


MWR: Microwave Radiometer for the Juno Mission to Jupiter

M.A. Janssen¹  · J.E. Oswald¹ · S.T. Brown¹ · S. Gulkis¹ · S.M. Levin¹ · S.J. Bolton² · M.D. Allison³ · S.K. Atreya⁴ · D. Gautier⁵ · A.P. Ingersoll⁶ · J.I. Lunine⁷ · G.S. Orton¹ · T.C. Owen⁸ · P.G. Steffes⁹ · V. Adumitroaie¹ · A. Bellotti⁹ · L.A. Jewell¹ · C. Li¹ · L. Li¹⁰ · S. Misra¹ · F.A. Oyafuso¹ · D. Santos-Costa² · E. Sarkissian¹ · R. Williamson¹ · J.K. Arballo¹ · A. Kitiyakara¹ · A. Ulloa-Severino¹ · J.C. Chen¹ · F.W. Maiwald¹ · A.S. Sahakian¹ · P.J. Pingree¹ · K.A. Lee¹ · A.S. Mazer¹ · R. Redick¹ · R.E. Hodges¹ · R.C. Hughes¹ · G. Bedrosian¹ · D.E. Dawson¹ · W.A. Hatch¹ · D.S. Russell¹ · N.F. Chamberlain¹ · M.S. Zawadski¹ · B. Khayatian¹ · B.R. Franklin¹ · H.A. Conley¹ · J.G. Kempenaar¹ · M.S. Loo¹ · E.T. Sunada¹ · V. Vorperion¹ · C.C. Wang¹

Received: 2 November 2016 / Accepted: 11 March 2017
© Springer Science+Business Media Dordrecht 2017

Abstract The Juno Microwave Radiometer (MWR) is a six-frequency scientific instrument designed and built to investigate the deep atmosphere of Jupiter. It is one of a suite of instruments on NASA's New Frontiers Mission Juno launched to Jupiter on August 5, 2011. The focus of this paper is the description of the scientific objectives of the MWR investigation along with the experimental design, observational approach, and calibration that will achieve these objectives, based on the Juno mission plan up to Jupiter orbit insertion on July 4, 2016. With frequencies distributed approximately by octave from 600 MHz to 22 GHz, the MWR will sample the atmospheric thermal radiation from depths extending from the ammonia cloud region at around 1 bar to pressure levels as deep as 1000 bars. The primary scientific objectives of the MWR investigation are to determine the presently unknown dynamical properties of Jupiter's subcloud atmosphere and to determine the global

✉ M.A. Janssen
michael.a.janssen@jpl.nasa.gov

- ¹ Jet Propulsion Laboratory, California Institute of Technology, 4800 Oak Grove Drive, Pasadena, CA 91109, USA
- ² Southwest Research Institute, 6220 Culebra Rd, San Antonio, TX 78228, USA
- ³ Goddard Institute for Space Studies, 2880 Broadway, New York NY 10025, USA
- ⁴ University of Michigan, 2445 Hayward St, Ann Arbor MI 48109, USA
- ⁵ Observatoire de Paris-Site de Meudon, Meudon Cedex, France
- ⁶ California Institute of Technology, 1200 E. California Blvd, Pasadena, CA 91125, USA
- ⁷ Cornell University, 402 Space Sciences Bldg, Ithaca, NY 14853, USA
- ⁸ Institute for Astronomy, University of Hawaii, Honolulu, HI 96822, USA
- ⁹ Georgia Institute of Technology, 777 Atlantic Dr NW, Atlanta, GA 30332, USA
- ¹⁰ University of Houston, 4800 Calhoun Rd, Houston TX 77004, USA

abundance of oxygen and nitrogen, present in the atmosphere as water and ammonia deep below their respective cloud decks. The MWR experiment is designed to measure both the thermal radiation from Jupiter and its emission-angle dependence at each frequency relative to the atmospheric local normal with high accuracy. The antennas at the four highest frequencies (21.9, 10.0, 5.2, and 2.6 GHz) have $\sim 12^\circ$ beamwidths and will achieve a spatial resolution approaching 600 km near perijove. The antennas at the lowest frequencies (0.6 and 1.25 GHz) are constrained by physical size limitations and have 20° beamwidths, enabling a spatial resolution of as high as 1000 km to be obtained. The MWR will obtain Jupiter's brightness temperature and its emission-angle dependence at each point along the subspacecraft track, over angles up to 60° from the normal over most latitudes, during at least six perijove passes after orbit insertion. The emission-angle dependence will be obtained for all frequencies to an accuracy of better than one part in 10^3 , sufficient to detect small variations in atmospheric temperature and absorber concentration profiles that distinguish dynamical and compositional properties of the deep Jovian atmosphere.

Keywords Jupiter · Microwave radiometry · Synchrotron emission · Atmosphere · Atmospheric composition · Atmospheric dynamics

1 Introduction

Jupiter is the most accessible of the outer planets and its atmosphere has been studied extensively from Earth and Space-based platforms. Because of the ubiquitous clouds that shroud the planet, however, such studies have been mostly limited to its properties in and above the cloud tops, and major questions remain about the composition and dynamical properties of the great bulk of the atmosphere that lies beneath. Other than Earth-based observations of deep thermal microwave emissions that can penetrate the clouds, we have had limited access to the subcloud atmosphere. Valuable insights have been gained about the deep atmosphere from measurements localized in time and space; e.g., the Galileo probe (Niemann et al. 1996; Folkner et al. 1998; Wong et al. 2004), glimpses into 5 μm hot spots (Bjoraker et al. 2015), the Shoemaker-Levy impact (Harrington et al. 2004) and observations of lightning. The information needed to synthesize these into a global picture of atmospheric processes beneath the clouds is lacking, however.

Thermal microwave emission from the deep atmosphere has been measured extensively using Earth-based instruments. Early on, this approach established a thermal microwave spectrum for the disk-integrated emission of Jupiter that demonstrated the long-wavelength thermal signature of deep convective atmospheres with an adiabatic lapse rate and ammonia gas as the principal microwave absorber (e.g., Field 1959; Gulkis et al. 1969; Wrixon et al. 1971; Gulkis and Poynter 1972; Berge and Gulkis 1976). However, as shown by de Pater et al. (2005), the ground-based brightness temperature spectrum is difficult to interpret in terms of its deep composition, even if the measurement accuracy throughout the spectrum were to be as good as $\sim 2\%$. Causes of this difficulty include the need to account for the non-thermal synchrotron radiation that dominates the planet's emission at long wavelengths, as well as uncertainties in atmospheric structure, cloud properties, and the absorption coefficients of water and ammonia at the high temperatures and pressures of the deep atmosphere. Dynamical properties such as the depth of the zones, belts, and other visible surface features are particularly difficult to observe from the Earth and remain a mystery. The resolution needed to observe spatial structure from the Earth requires large interferometric arrays; however, the Earth-rotational aperture synthesis approach they require

has made longitudinal structure difficult to observe until recently. Longitudinally-averaged belt/zone variations attributed to varying ammonia distribution have been observed at wavelengths from 2 to 6 cm using the Very Large Array in New Mexico (de Pater and Dickel 1986; de Pater et al. 2001), while observations at 2-cm wavelength made synchronously with the rotations of Jupiter and the Earth have enabled longitudinal structure to be identified along with banding (Sault et al. 2004). In conjunction with the Galileo probe measurements these have led to interesting speculations on the subcloud ammonia depletion and its implications for deep circulations (de Pater et al. 2001; Showman and de Pater 2005). While recent upgrades to the VLA have dramatically improved its ability to image Jupiter at short wavelengths (corresponding to pressures less than about 3 bars, de Pater et al. 2016), the resolution and sensitivity limitations of observations previous to this have limited their usefulness.

Progress toward understanding Jupiter's deep atmosphere from a global perspective requires microwave observations with better calibration that extend into the long-wavelength end of the spectrum as far as possible to see deep into the atmosphere. The space-based approach of the Juno mission overcomes many of the main limitations in the microwave remote sensing of Jupiter's atmosphere. Juno's highly eccentric orbit with its close equatorial perijove allows Jupiter's atmosphere to be observed from inside the surrounding radiation belts, simplifying the job of separating the synchrotron from atmospheric thermal emission. Observations from close range allow good spatial resolution to be achieved on Jupiter at all wavelengths, and, in particular, allow observations to be made at the very long wavelengths needed to sound the atmosphere deep below the ammonia and water cloud regions. Although complete global mapping is not obtained, the polar orbit allows the detailed structure with latitude to be examined from equator to pole. With careful attention to beam pattern knowledge and radiometer stability, the Juno orbit and spin orientation also makes it possible to measure the emission-angle dependence of the thermal emissions with high accuracy. The accurate measurement of relative brightness temperature as a function of off-nadir emission angles is a powerful approach to obtaining atmospheric parameters by multi-frequency sounding (Janssen et al. 2005). The results from Juno will surpass those from all existing observations in spatial resolution, accuracy, and frequency coverage.

2 Science Objectives

The overarching goal of the Juno mission is to understand the origin of Jupiter. Juno will accomplish this goal largely by determining the atmospheric composition, existence and mass of the core and structure of the internal magnetic field. The microwave radiometer instrument (MWR) makes a vital contribution to this goal by determining the bulk abundance of water and studying atmospheric dynamics. In the process, MWR measurements will also allow a better understanding of Jupiter's complex radiation environment. We elaborate on these MWR objectives in the following subsections.

2.1 Global Water Abundance

Oxygen is the third most abundant element on the Sun, after hydrogen and helium (Asplund et al. 2009), so water is the most abundant compound after H₂ in a planet with solar elemental ratios. In terms of the planet's bulk density and the C/H ratio determined from the methane abundance, Jupiter comes closest of all the planets to this ideal solar composition

mixture. All four giant planets are relatively enriched in heavy elements. For instance, Saturn's C/H ratio is about 10 times the protosolar value, while Jupiter's is about 4.0 times the protosolar value (Atreya et al. 2017). The protosolar value is used rather than the current value to account for the loss of hydrogen during nuclear fusion within the Sun. Despite the high enrichment ratios, the absolute abundances are small—the C/H protosolar mixing ratio is only 2.65×10^{-4} , for instance. The Galileo probe measured Jupiter's atmospheric composition down to the 22-bar pressure level (Niemann et al. 1998; Folkner et al. 1998; Mahaffy et al. 2000). For Jupiter the enrichment factors relative to the Sun measured by the probe for C, N, and S are 4.0, 4.5, and 3.1, respectively, but for O the enrichment factor is only 0.46. These numbers are derived from the abundances of CH₄, NH₃, H₂S, and H₂O. Thus the water abundance is the big discrepancy.

One could imagine processes that would enrich all of these elements in similar amounts (Atreya et al. 2017). During their first few million years, stars like the Sun are extremely active, with intense stellar winds that are capable of separating the gases from the solids in the solar nebula. Beyond the ice line, sufficiently far from the Sun, CH₄, NH₃, H₂S, and H₂O form into solid ice particles that are able to withstand the solar wind pressure while the dominant constituents, the gases like H₂ and He are blown away. However this would produce similar enrichment factors for C, N, S, and O, and that is not what the Galileo probe observed. There is also a meteorological explanation for the low abundance of O. The Galileo probe entered a 5-micron hot spot—a clear space with no clouds and reduced mixing ratios of NH₃, H₂S, and H₂O where their clouds should have been. The mixing ratios of NH₃ and H₂S increased at deeper levels and finally leveled off at their enriched values before the probe died at 22 bars, but the H₂O was still climbing and never rose above the 0.46 enrichment factor quoted above. Either the probe entered a dry spot or Jupiter itself is anomalously dry. The latter would overturn our ideas about chemical processes during planet formation, so measuring the global water abundance is an important objective of the MWR instrument.

An enrichment factor for water similar to those for CH₄, NH₃, and H₂S would help solve another puzzling feature of the Galileo probe results, namely the enrichment factors of Ar, Kr, and Xe, which are in the range 2.3–3.3 and therefore similar to the enrichment factors of C, N, and S. The noble gases are hard to separate from H₂ and He in the solar nebula. As gases they would tend to get blown away with the H₂ and He, leaving them with enrichment factors of 1.0. One theory (Owen et al. 1999; Atreya et al. 2002) is that all the heavy gases condensed to form ices out beyond Neptune at temperatures below 30 K and came in later as icy comets when the Sun had quieted down. Another theory (Lunine and Stevenson 1985; Gautier et al. 2001; Hersant et al. 2004) is that the heavy gases were incorporated locally into clathrate hydrates. This hypothesis requires water enrichment greater than 10 because the number of sites in the clathrate lattice is finite. Water is probably the transport medium for delivering volatiles to the inner solar system as well. Whether the water is cometary (Owen et al. 1992; Owen and Barnum 1995) or asteroidal (Marty 2012; Altwegg et al. 2015; Barnes et al. 2016) is still an open question. Thus the MWR measurement is relevant to understanding volatile processing throughout the early solar system.

Water is also important to understanding the radial distribution of elements in Jupiter's interior and therefore the planet's formation history. The prevailing view is that a 10–20 Earth mass “seed” of heavy elements was necessary to attract hydrogen and helium in the solar nebula and form a giant planet (e.g., Pollack et al. 1996). The seed became the core, but the fraction of heavy elements in the core compared with that in the gaseous envelope is uncertain, which bears on the sequence of events as the planets were forming. Much of this information is in the gravity field, which Juno will measure, but a key boundary condition is

the water abundance at the top of the envelope. MWR will measure water in the 10–100+ bar range, which is only 0.3% of the distance to the center of Jupiter, but it is thought to be representative of the global water abundance since the planet is likely stirred by convection down to the core.

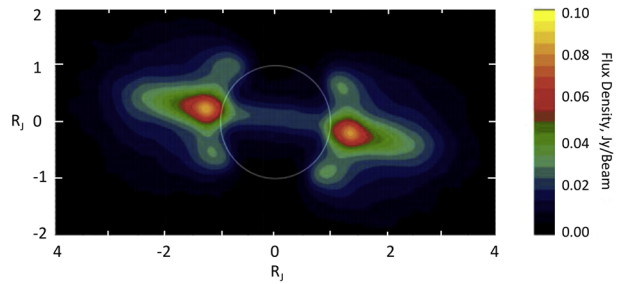
2.2 Atmospheric Dynamics

Little is known about dynamical and chemical processes in the subcloud region of the Jovian planets, and a major objective of the MWR experiment is to better understand them. The MWR data will uniquely address the spatial variation of ammonia and water down to depths greater than 100 bars, or over 300 km below the base of the ammonia cloud. Except for the Galileo probe, which reached a pressure of nearly 22 bars at one location on the planet, our direct knowledge of the atmospheric dynamics is two-dimensional and confined to the tops of the ammonia clouds and above. By comparing the variations of ammonia and water below the clouds with visible cloud-top features, the MWR will help distinguish between a deep atmosphere gently stirred by convection and one in which high-speed jet streams extend into the deep interior. The belts and zones are the dark and light bands that circle the planet at constant latitude. Their boundaries coincide with the peaks of eastward and westward jets with speeds of ~ 50 – 100 m/s. Evidence of lightning, towering convective clouds, and molecules out of chemical equilibrium with their surroundings suggest large-scale vertical motion, somewhat like the Hadley cells on Earth. How deep these vertical motions extend is unknown, but the MWR will explore the possibilities. If the deep ammonia and water distributions are correlated with the belts and zones, then the large-scale circulation is deep. If the deep ammonia and water abundances are constant, then the weather that we see is probably confined to a thin atmospheric layer. The MWR data will provide an essential constraint on general circulation models (GCMs, e.g., Heimpel et al. 2016; Thomson and McIntyre 2016; Liu and Schneider 2010, 2015; Sugiyama et al. 2014; Lian and Showman 2010; Vasavada and Showman 2005). The vertical motions, about which we have so little information, are the key to understanding what maintains the large-scale circulation—how mechanical energy is created, how it is transferred to the large scales, and how it is dissipated. The spatial distribution of the condensates water and ammonia depend on vertical motion through the cycles of evaporation, precipitation, and latent heat release. They respond to convection, which is an intense, small-scale process that strongly affects the large-scale circulation. Therefore, the distribution of these gasses provides a window for investigating the mechanical energy cycle of giant planet atmospheres. Such a cycle (Lorenz 1955) has already been used to understand the atmospheric systems and climate changes on terrestrial planets and satellites (Peixoto and Oort 1992; Schubert and Mitchell 2013; Lucarini et al. 2013; Tabataba-Vakili et al. 2015). However, we have little information about the energy cycle of the atmospheres on either Jupiter or Saturn.

2.3 Radiation Belts

Synchrotron emission from relativistic electrons in Jupiter's radiation belts is a source of contamination for microwave observations of the atmosphere. It is also a valuable source of information about the distribution of the most energetic electrons trapped in Jupiter's inner magnetosphere. Ground-based microwave observations coupled with *in situ* measurements of the electron distribution have been used to adjust models of the radiation belts (Garrett et al. 2005), but the spatial resolution is limited. Furthermore, synchrotron emission is beamed in the direction of electron motion, which is inextricably linked to the magnitude and

Fig. 1 Jupiter's synchrotron emission imaged by the VLA at 1.4 GHz (Levin et al. 2001). The peak brightness temperature at this frequency is roughly 1000 K



direction of the Jovian magnetic field as well as the energy of the electrons. From Earth, we can only observe Jupiter from a limited range of angles, all within ~ 13 degrees of Jupiter's magnetic equator. As a trapped electron spirals along a magnetic field line, it spends most of its time near the "mirror point", where it reverses direction with a pitch angle of 90° , and the bulk of the Jovian synchrotron emission seen from Earth comes from electrons mirroring on magnetic field lines which are perpendicular to the line of sight. Thus, information about the energy distribution of the electrons is entangled with information about their pitch-angle distribution, and complicated by the structure of Jupiter's magnetic field.

The MWR on Juno will not suffer from this limitation. With each spin of the spacecraft, MWR will observe the synchrotron emission at each of six frequencies, over a wide range of angles, from a unique vantage point inside the radiation belts. Furthermore, the magnetometer experiment on Juno will be making an improved map of the Jovian magnetic field (Connerney et al. 2017). The peak frequency of the synchrotron spectrum is proportional to energy times the magnetic field strength, so the MWR frequencies are sensitive to different electron energies throughout the belts. As seen in Fig. 1, observations with the VLA show strong emission near the equator, implying a "pancake" distribution of electrons with equatorial pitch angle close to 90 degrees, plus high-latitude lobes that require a component with a more isotropic distribution of pitch angles near an L-shell value of 2 (the set of parallel magnetic field lines that cross Jupiter's equator at two Jovian radii). The relative absence of emission at intermediate latitudes adds complexity, requiring either a more complicated pitch-angle distribution or an energy distribution that depends on both pitch angle and L-shell. Juno's trajectory will take it over the poles, in between the high-latitude lobes and the equatorial region, and close to the planet at the equator, allowing both the high latitude lobe and the equatorial lobe regions to be observed at a wide range of angles with respect to the magnetic field, including both parallel and perpendicular to the field lines. Observations at multiple frequencies from this wide range of vantage points, combined with a precise map of the magnetic field and ground-based measurements, will allow us to disentangle the energy and pitch angle distributions from the geometry and strength of the magnetic field.

3 Measurement Objectives

The measurement objectives depend on both the capabilities of the measurement system and the characteristics of the observed source (or sources in this case). After describing our program for the forward modeling of microwave emission from Jupiter's atmosphere and its radiation belts, we explore the characteristics of these emissions in order to understand the requirements for a microwave measurement system that can best capture the information contained in them.

3.1 Jovian Models

3.1.1 Atmospheric Model

Shortly after the selection of the Juno Mission, work started on the development of a software model of the Jovian atmosphere that could be used by the Juno MWR instrument team and other investigators for use in observation planning and estimating instrument responses, and for developing data analysis techniques to interpret the MWR data. Atmospheric composition for this early work assumed a He to H₂ ratio of 0.157 and a CH₄ molar mixing ratio of 1.8×10^{-3} consistent with values given by Atreya et al. (1999). Microwave opacity sources included H₂O, NH₃, H₂, and a liquid water cloud. The mixing ratios of NH₃ and H₂O in the fully mixed region of the atmosphere were assumed to be variable, ranging from 3 to 5 times solar abundances for ammonia, and 1 to 9 times solar for water. No loss of NH₃ into a water cloud or a possible NH₄SH cloud was considered. At the beginning it was already clear that additional work was needed that used a wider range of parameters and model assumptions, and a design that made it amenable to the use of software modules for carrying out inverse calculations to determine the water and ammonia abundances in the Jovian atmosphere from MWR measurements. These were all motivating factors for developing the MWR forward model, now called the Jupiter Atmospheric Radiative Transfer model, or JAMRT for short.

The JAMRT program describes a deep convective model atmosphere adequate for the interpretation of MWR observational data. Pressures included in the model range from 0.3 bars to one kilobar. JAMRT computes temperature, gas composition, and cloud density profiles as functions of pressure and altitude, optionally based on either the ideal gas equation of state or a real equation of state for the mixture using thermodynamic relationships. Hydrostatic equilibrium (including solid body rotation) is assumed to exist throughout the model. The atmosphere is stratified along a direction normal to the gravity equipotential surfaces of Jupiter (e.g., Lindal et al. 1981). The shape of Jupiter's atmosphere is assumed to follow an equipotential surface based on up-to-date spherical harmonic measurements of the Jupiter's gravity field. Local gravity is a (variable but definable) parameter in the model, thus allowing one to compute atmospheric profiles at any specified latitude. Local gravity can be calculated assuming Jupiter to be a gaseous body, uniformly rotating and in hydrostatic equilibrium. Upper tropospheric winds that vary with latitude may be included in the potential model. Non-uniform stratified layer thicknesses can be specified by the user. Moist and dry adiabatic lapse rates, subadiabatic lapse rates, and specified relative humidity (RH) within the cloud are user-defined options. The dry atmosphere is composed of H₂, He, CH₄, PH₃ and noble gases as measured by the Galileo entry probe. The condensable gases are H₂O, H₂S, and NH₃. The condensates are H₂O ice, H₂O liquid, NH₃/H₂O solution, NH₄SH ice, and NH₃ ice. Vapor pressures and moist adiabats for these gases and condensates are given in Atreya (1986) and elsewhere. The current (nominal) atmospheric composition in solar abundances relative to H₂ and enrichments given in Table 1 are based on Atreya et al. (2017). The mixing ratios (mole fractions) of the constituents are given in column 4. State-of-the-art microwave absorption coefficients are used for all atmospheric components, although only NH₃ and H₂O gas have been found to be significant for the interpretation of microwave data. A laboratory program focused on the determination of NH₃ and H₂O microwave absorption coefficients that cover the pressure-temperature range probed by the MWR is described in Sect. 3.1.2.

The model atmosphere must simultaneously satisfy boundary conditions at the top and bottom of the atmosphere. At the deepest level, which might be several hundred bars up to 1000 bar, the user specifies the molar mixing ratios of water and ammonia. At the highest level, which is usually 0.3 bars, the temperature must agree with direct measurements.

Table 1 Protosolar and nominal atmospheric abundances for JAMRT

Species	Protosolar abundance relative to H ₂ ^a	Enrichment (Jupiter/Protosolar)	Jupiter mole fraction ^b
H ₂	1		0.862
He	0.191	0.82	0.135
CH ₄	5.90×10^{-4}	4.02	2.04×10^{-3}
H ₂ O	1.07×10^{-3}	0.46	4.22×10^{-4}
NH ₃	1.48×10^{-4}	4.48 ^c	5.72×10^{-4c}
H ₂ S	2.90×10^{-5}	3.08	7.67×10^{-5}
Ar	5.50×10^{-6}	3.31	1.57×10^{-5}
PH ₃	5.64×10^{-7}	3.83	1.86×10^{-6}

^aProtosolar values are calculated using photospheric values from Asplund et al. (2009), as described in Atreya et al. (2017)

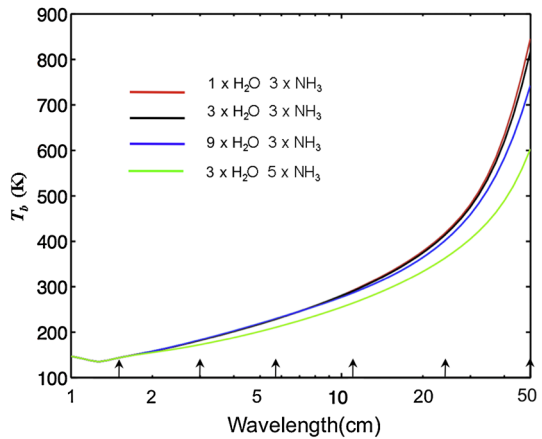
^bBased on the Galileo Probe Mass Spectrometer (GPMS) data, except for PH₃, which was derived from Cassini flyby of Jupiter (see Atreya et al. 2017 and references therein)

^cNH₃ mole fraction of 7×10^{-4} , or Jupiter/Protosolar = 5.4, was derived from analysis of the attenuation of Galileo probe radio signal (see Atreya et al. 2017 for additional details)

Typically, we take the user specified (T , P) point to be (132.79 K, 0.50 bar) based on measurements near 6.53°N. latitude with the Galileo entry probe (Seiff et al. 1998). To satisfy both sets of boundary conditions, the user makes an initial guess about the temperature at the maximum pressure. The program proceeds to build a model atmosphere starting from the maximum pressure and assumed initial temperature and composition at this pressure. When the atmosphere reaches the preset pressure level near the top of the atmosphere, it compares the temperature of the model with the preset temperature. If the model pressure-temperature point agrees with the preset point, the model building stops. If the two are different, the temperature at the bottom of the atmosphere is changed and a new model atmosphere is calculated. An iterative approach is used until the initial conditions at the bottom of the atmosphere lead to the preset pressure and temperature at the top of the atmosphere by integrating upward.

The standard model assumes uniform mixing until saturation occurs, and then follows a saturation law that depends on the cloud model. Cloud bases are defined as the pressure where the partial pressure of a condensable gas is equal to a user-specified RH times the saturation vapor pressure of the gas. Within the cloud, the lapse rate is a user-specified fraction of the moist adiabatic lapse rate, and the relative humidity of condensable gases can be modeled as constant, linear, or quadratic functions of pressure. Figure 2 shows plots for the nadir brightness spectra of several atmospheric models with different compositions. These use the same nominal assumptions about the atmospheric structure, such as uniform concentrations of the dominant microwave absorbers H₂O and NH₃ below their respective saturation points, with 100% humidity above this point, and the use of wet adiabats at all altitudes. NH₃ and H₂O are by far the most dominant microwave absorbers in Jupiter's atmosphere, while NH₃ has about an order of magnitude more opacity than H₂O. Variation of the H₂O concentration by an order of magnitude makes a small difference only apparent in the spectra at the longest MWR wavelengths, while the modest change in NH₃ concentration from 3 to 5 X solar makes differences of several percent. We anticipate that the distribution of ammonia throughout Jupiter's atmosphere will be readily achieved with brightness tem-

Fig. 2 Absolute nadir brightness temperature spectra for models with different concentrations of NH_3 and H_2O . The curves indicate the respective model concentrations of each constituent in proportion to the solar abundances given in Table 1. The arrows on the abscissa indicate the MWR wavelengths



perature spectra alone, while water will require a more sophisticated approach as discussed later.

3.1.2 Supporting Measurements

In order to enable accurate interpretation of data from high-precision observations by the Juno Microwave Radiometer, over 6000 laboratory measurements of the microwave absorption properties of gaseous ammonia, water vapor, and aqueous ammonia solution have been conducted under simulated Jovian conditions using new laboratory systems capable of high-precision measurement under the extreme conditions of the deep atmosphere of Jupiter (up to 600 bars and 600 K). This is one of the most extensive laboratory measurement campaigns ever conducted in support of a microwave remote sensing instrument, and is described in Steffes et al. (2017) (see also Morris and Parsons 1970; Hanley et al. 2009; Devaraj et al. 2014; Bellotti et al. 2016). New, more precise models for the microwave absorption from these constituents have been developed from these measurements. Application of these absorption properties to radiative transfer models for the six wavelengths involved provides a valuable tool for planning observations, and will also make possible accurate retrievals of the abundances of these constituents.

This laboratory program consisted of five campaigns, using three different laboratory systems. The first, referred to as the “medium-pressure” system, was used for measurements of the 1.1–20 cm wavelength (1.5–27 GHz) opacity of ammonia in a hydrogen/helium atmosphere at pressures up to 12 bars and temperatures from 185–450 K (Hanley et al. 2009). The second system, referred to as the “high-pressure” system, was used for measurements of the 5–21 cm wavelength (1.4–6 GHz) opacity of water vapor in a hydrogen/helium atmosphere at pressures up to 101 bars and temperatures up to 505 K (results discussed in Karpowicz and Steffes 2011a, 2011b). Subsequently the same high-pressure system was used to conduct measurements of the 5–21 cm wavelength (1.4–6 GHz) opacity of gaseous ammonia in a hydrogen/helium atmosphere at pressures up to 98 bars and temperatures up to 503 K (results discussed in Devaraj et al. 2014). Of special note was the use of this system to conduct the first measurements of the effects of water vapor broadening on the centimeter-wavelength absorption spectrum of ammonia (Devaraj et al. 2014). A final set of measurements using this system was conducted of the 5–21 cm wavelength (1.4–6 GHz) opacity of pure ammonia and of pure water vapor conducted at 600 K and lower pressures

(Bellotti et al. 2016). A third system was used for measurements of the 3.5–15 cm wavelength (2–8.5 GHz) complex dielectric properties of aqueous ammonia, the putative liquid cloud constituent in the Jovian atmosphere (Duong et al. 2014).

3.1.3 Synchrotron Model

In preparation for Jupiter observations, our synchrotron modeling effort is predominately focused on enabling subtraction of the synchrotron emission to achieve the required accuracy for atmospheric measurements. We have two independent models, each capable of producing a synchrotron emission map which predicts the MWR observations on orbit, and each consistent with the Earth-based observations of synchrotron emission. The simpler model (Adumitroaie et al. 2016; Levin et al. 2001) uses an ad hoc 4-parameter pitch angle distribution adjusted for each of eight zones in L-shell, producing an equatorial main belt and high-latitude lobes that match the VLA observations (Fig. 1). This model enables relatively rapid adjustment to match direct MWR observations of the synchrotron emission. The more complex model (Santos-Costa and Bolton 2009; Santos-Costa et al. 2014) attempts to incorporate all known physics of transport mechanisms and interactions within the radiation belts, but will be more cumbersome to adjust in response to observations.

3.2 Observational Parameters for Juno

3.2.1 Frequency Coverage

The region of Jupiter's atmosphere targeted for exploration of its compositional and dynamical properties extends downward from the ammonia cloud region to strictly unknown depths. Figure 3 shows the brightness temperature contribution functions computed for the

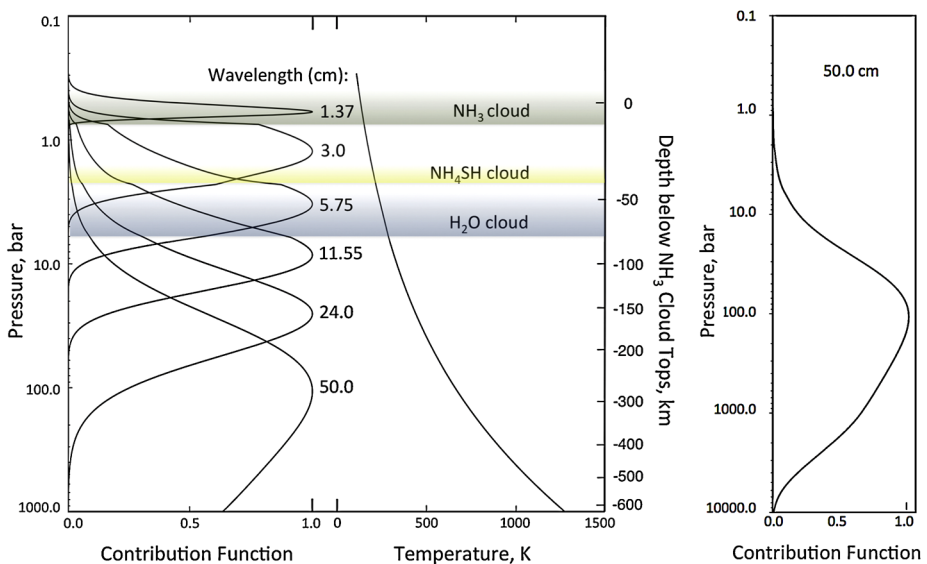


Fig. 3 Contribution functions vs. pressure in a nominal Jupiter atmosphere at the indicated MWR wavelengths

six MWR channels using our radiative transfer model and an assumed atmosphere containing nominal concentrations of ammonia and water (3 X solar each). The contribution function is related to the usual form of the weighting function as it appears in the solution to the one-dimensional atmospheric radiative transfer function. In the case of a radiometer viewing along a line of sight s through a non-scattering medium characterized by temperature and absorption coefficients known as a function of s , we may write (Janssen 1993)

$$T_b = \int_0^{\infty} W(s)T(s)ds \quad (1)$$

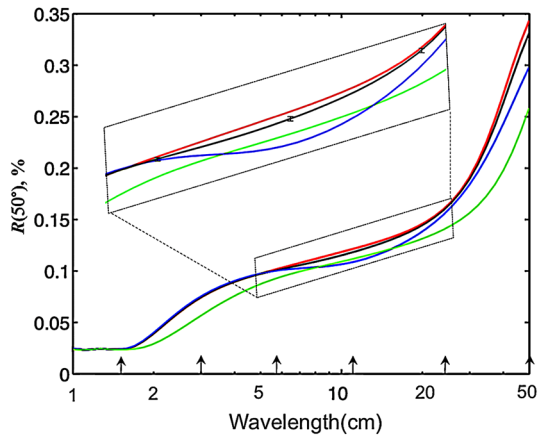
where T_b is the brightness temperature seen by the observer, $T(s)$ is the physical temperature of a non-scattering but absorptive medium along a ray path s , and the details relating to the absorptive properties of the medium are contained in the weighting function W (e.g., such properties would include local gravity, temperature and pressure, mixing ratios and microwave absorption coefficients). For a deep atmosphere spanning orders of magnitude in pressure, it is more descriptive to plot this in terms of logarithmic pressure and include the temperature, namely

$$T_b = \int_0^{\infty} C(s) d \log P \quad (2)$$

where C is the contribution function derived from Eq. (1). In this form the contribution to the brightness temperature T_b from a range in pressure can be visualized as proportional to the area of the plotted contribution function between the two pressures. In this formulation we can see that the contribution functions are approximately symmetric in $\log P$ for channels 2 through 6 (24 to 1.37 cm), with peaks around 30, 10, 3.5, 1.5 and 0.7 bars respectively. The highest frequency lies in the center of the strong ammonia 1-cm band, and the remaining frequencies were chosen to provide overlapping weighting functions descending as far as feasible into Jupiter's depths. This was achieved by decreasing the successive frequencies by octaves. The lowest frequency was dictated by aperture size considerations inasmuch as a minimum of a few wavelengths diameter is required to provide angular resolution; furthermore, the rapid increase in the brightness of the synchrotron emission from the radiation belts makes narrow beams more important in order to isolate the atmospheric emissions.

The interpretation becomes more difficult at the lowest frequency where the contribution function descends deep into a temperature and pressure regime where the microwave properties of a Jovian-type atmosphere remain untested by laboratory measurements. The choice of 600 MHz (50-cm wavelength) allowed an acceptable compromise that allows us to explore the deepest region of Jupiter accessible by the Juno mission. This channel is different because the absorption of ammonia and water change character at pressures higher than ~ 100 bar and the contribution function descends to much deeper levels than would be expected based on the behavior seen at the five higher-frequency channels. The right panel shows the channel 1 contribution function over nearly its full range in pressure. Because of the asymmetry in pressure, the median contribution centers on a pressure level of ~ 200 bars, well below its peak, and shows significant ($>20\%$) contribution from levels below 1000 bar. While almost all of the contribution to brightness temperatures in channels 2 through 6 comes from pressures above 100 bar and therefore within the range of laboratory measurements, most of the contribution to the channel 1 brightness temperatures depends on extrapolations by as much as two orders of magnitude in pressure beyond the laboratory measurements, and to temperatures in excess of 2000 K. While structure seen at this lowest frequency is very important, its interpretation will have a different character than that from the other channels. For example, the presence of structure in channel 1 not seen in channels 2 and 3, or conversely the absence of structure in channel 1 seen in these channels would be of interest even if the absolute opacity is uncertain.

Fig. 4 Spectra of the limb-darkening parameter as a function of wavelength across the MWR measurement range, for a nominal atmospheric model with mixing ratios relative to solar of 3 X and 5 X solar for ammonia and 1 X, 3 X, and 10 X solar for water. The arrows on the abscissa indicate the MWR channels. The insert shows a blowup of the indicated region of the plot with the currently expected measurement uncertainties for the MWR (see Table 7) plotted on the 3 X solar water curve



3.2.2 Emission-Angle Dependence

In principle the microwave spectrum of Jupiter contains all the information that can be obtained on composition and thermal structure from microwave remote sounding. It is difficult to take advantage of this because, as Fig. 3 illustrates, the spectral range needed extends over many octaves of frequency. As pointed out most recently by de Pater et al. (2005) and Janssen et al. (2005), important spectral features that discriminate among uncertain properties of the atmosphere lie below the level of uncertainty inherent in the absolute calibration across such a broad frequency range. The capability for the absolute calibration of Jupiter's microwave spectrum is currently much improved although still greater than 1% (Perley and Butler 2013), and can determine important properties of Jupiter's atmosphere such as its ammonia content. The emission-angle dependence is essentially the derivative of the spectrum and contains the same information; however, as proposed by Janssen et al. (2005) and demonstrated in this paper, it can be measured with greater accuracy (i.e., 1 part in 10^3) and is capable of discriminating among cases that the spectral measurements can't. Our approach has been to require the most accurate microwave measurements of Jupiter that are experimentally feasible, which include the capability for limb darkening as well as spectral measurements.

Following the approach in Janssen et al. (2005), we define the limb darkening parameter

$$R(\theta) = \left(\frac{T_b(0) - T_b(\theta)}{T_b(0)} \right) \quad (3)$$

where $T_b(\theta)$ is the brightness temperature of Jupiter at an angle θ from the nadir direction ($\theta = 0$). Figure 4 shows a plot of the limb darkening parameter for the same models depicted in Fig. 2. The limb-darkening spectrum considered in this paper assumes a limiting emission angle θ that varies as a function of orbit and observing geometry as discussed in Sect. 5.2. Taking a nominal model with a subcloud ammonia mixing ratio (3 X solar) as a reference, we vary the subcloud water mixing ratio and examine its signature in the spectra of the limb darkening. The uncertainty in the radioastronomical flux scale across this frequency range has improved in recent years from about 5% (Baars et al. 1977; Kellerman 2009), with the potential of being improved to as good as 1% at the shorter wavelengths using planetary observations by the Wilkinson Microwave Anisotropy Probe (WMAP) (Partridge et al. 2016). Figure 2 shows that the nadir brightness temperature spectrum by itself can determine the ammonia content of the atmosphere, while we see in Fig. 4

that the measurement of limb darkening is capable of discriminating among important cases with more subtle spectral variations.

3.2.3 Synchrotron Measurements

The radiation belts will be observed as the antenna boresights rotate off Jupiter and view the synchrotron emission against the cold sky. The MWR measures a single linear polarization for each channel, while the synchrotron emission is partially polarized, which complicates the analysis. However, as the spacecraft moves along its trajectory and the antenna boresights sweep over the sky, the accumulated set of observations will observe synchrotron emission from the radiation belts over the full range of latitude and a very wide angular range with respect to the magnetic field at each location. For trapped relativistic electrons, the magnetic field line also introduces a local line of symmetry, both axially and upon reflection up or down the field line. It should therefore be possible to disentangle the effects of polarization, dependence of the energy distribution on electron pitch angle, and line of sight effects to determine the distribution of electrons.

3.3 Requirements on the MWR Instrument

The prospect of measuring the limb-darkening parameter R to an accuracy of 0.1% was the basis for setting the requirements for the design of the MWR experiment. No particular advance in the state-of-the-art was needed to achieve this level of performance; however, radiometric stability and antenna pattern characteristics had to be carefully controlled to limit the effect of experimental uncertainties. Overall, bandwidth-limited white noise and the drift of baseline and gain set requirements on both the experimental approach and the radiometer design, while antenna beamwidth and sidelobe performance set additional requirements on the observational approach and the antenna design. These considerations led to the establishment of requirements that were used by the Juno project to control the design and implementation of the MWR. The most significant ones were:

1. The MWR shall measure the microwave brightness temperature at each subspacecraft footprint with accuracy sufficient to determine the difference between nadir and off-nadir microwave brightness temperatures of Jupiter at each frequency, to a 1-sigma accuracy of 0.1% of the nadir brightness temperature, as averaged over 5 seconds of accumulated data, excluding uncertainties arising from longitudinal brightness variations, over the latitude and emission angle ranges specified in the second requirement.
2. The MWR shall measure the microwave brightness temperature at each subspacecraft footprint within the latitude range $\pm 50^\circ$ over a range of emission angles that include at least one angle less than 10° and one angle in the range 40° to 50° , with the accuracy specified in the first requirement.
3. The MWR antennas shall have beamwidths less than 22° , with a goal less than 12° .

An error budget was established at the outset to track the estimated performance of the design. Table 2 shows the initial allocations made for the overall receiver and antenna subsystem errors respectively as they affect the determination of the limb-darkening parameter R . The quantities in this table, the antenna temperature along with the antenna temperature and pattern corrections, are described in detail in Sect. 5. A detailed instrument and measurement error model enabled lower-level allocations to be made within each subsystem. This guided the level of effort placed on various elements of the instrument in its development, and ultimately evolved into the detailed instrument calibration plan described in Sect. 5.

Table 2 Instrument subsystem error allocations (units of R in percent)

	Ch1	Ch2	Ch3	Ch4	Ch5	Ch6
Measurement noise (5 s avg.)	0.038	0.039	0.036	0.042	0.042	0.048
Antenna temperature calibration (ATC)	0.053	0.052	0.046	0.067	0.059	0.068
Antenna pattern correction (APC)	0.075	0.075	0.060	0.060	0.060	0.050
Unallocated error	0.011	0.013	0.055	0.012	0.034	0.025
MWR requirement	0.100	0.100	0.100	0.100	0.100	0.100

The requirements on the instrument for the synchrotron emission measurements are more relaxed. Gain stability and calibration requirements are fully satisfied by the more stringent requirements set by the atmospheric observations. However, because the peak brightness temperatures of the synchrotron emission far exceed those from the atmosphere at the two lowest MWR frequencies, the receivers for these channels were designed to be capable of a dynamic range of more than an order of magnitude larger than that required for the higher-frequency channels.

4 MWR Instrument

4.1 General

The MWR instrument is divided into three main subsystems: (1) the microwave receivers, (2) the electronics subsystems contained in the spacecraft vault, and (3) the antennas, located on two external panels of the spacecraft, and including the transmission lines that connect the antennas to the receivers. Figure 5 shows a functional block diagram of the instrument. The MWR hardware is spread around the spacecraft—engineering perspective drawings in Fig. 6 show its configuration. The pointing axes of the antennas are perpendicular to the spacecraft spin axis so that the antenna beams sweep through a great circle on the sky as the spacecraft rotates. Figure 7 shows pictures taken of the assembled instrument prior to its delivery to spacecraft integration. By convention the six radiometer channel strings, each comprising antenna, transmission line, and receiver, are designated as C1 through C6 from lowest to highest frequency. The corresponding antennas and receivers are designated A1 through A6 and R1 through R6 respectively. Table 3 gives the nominal characteristics of each radiometer channel.

4.1.1 Receivers

The receiver subsystem comprises six direct-detection Dicke-switched radiometer receivers with integral noise diodes for short-term gain calibration. The receiver designs were based as far as possible on the Advanced Microwave Radiometer (AMR) flown on the Ocean Surface Topography Mission (OSTM) launched in 2008 (Brown 2013). The receiver characteristics are summarized in Table 3 and the overall receiver design is shown in Fig. 8. The upper end of the dynamic range specification for each channel was set to be at least two times the expected maximum antenna temperature from either the planet or synchrotron. Figure 9 shows a photograph of one of the receivers. An RF passband of about 4% is formed by two stages of microstrip bandpass filters designed to match the antenna passbands and to ensure

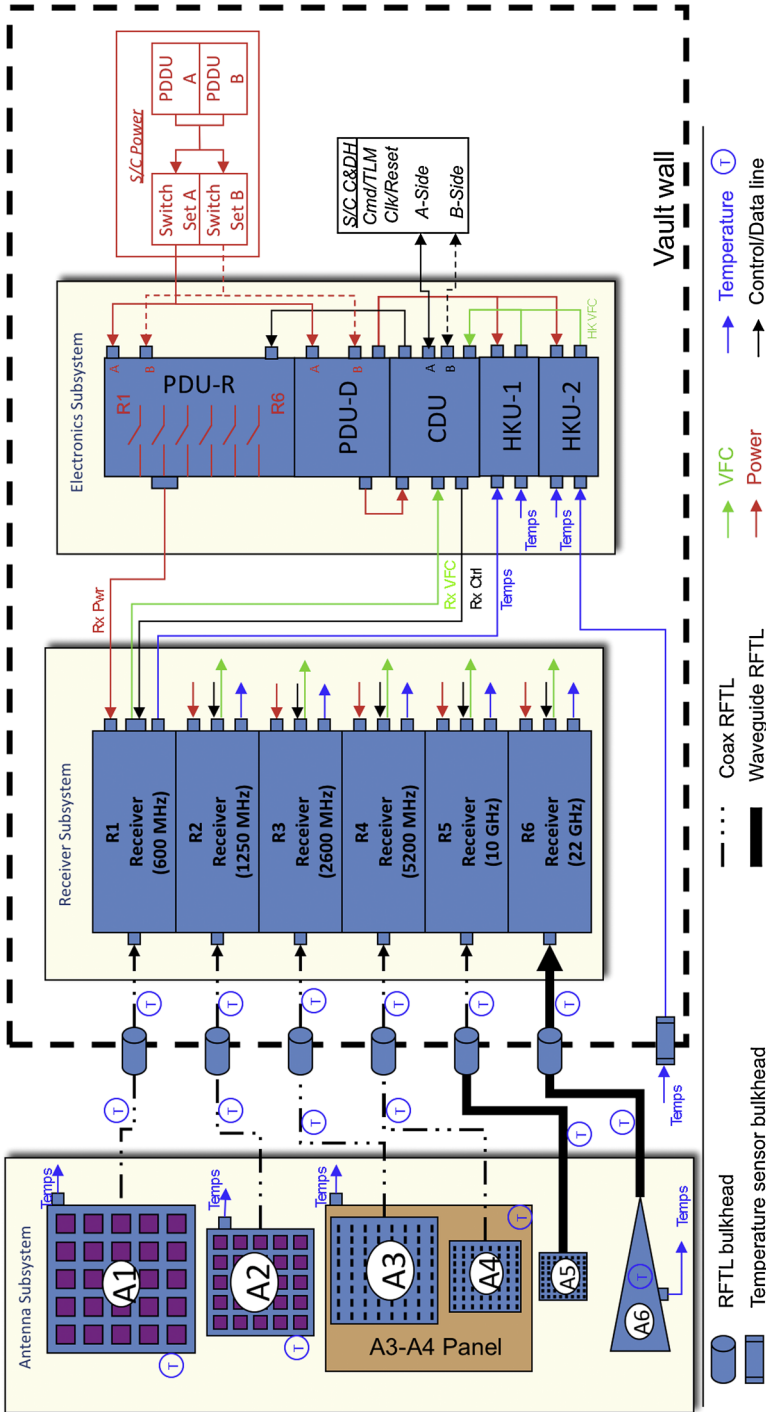


Fig. 5 MWR functional block diagram showing subsystems, left to right respectively: Antennas, Radio Frequency Transmission Lines (RFTLs), Receivers, and Electronics Unit (EU). The receivers and electronics are in a radiation-protected vault on the spacecraft

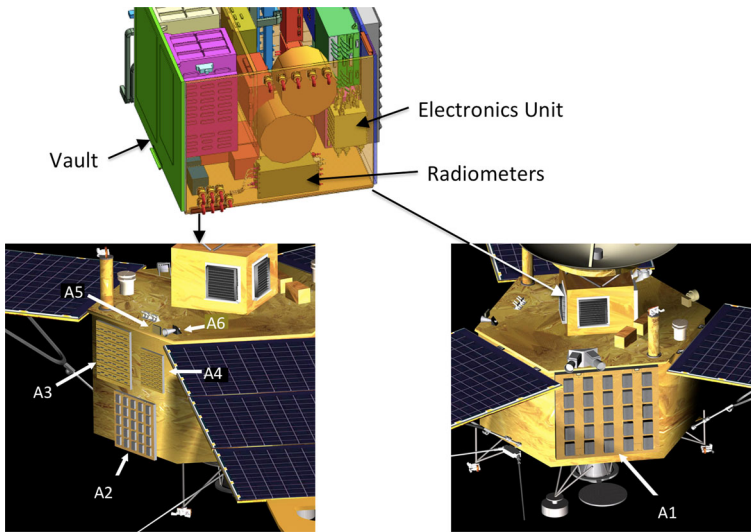


Fig. 6 MWR spacecraft configuration. The antennas are located on two sides of the spacecraft, all viewing perpendicular to the spacecraft spin axis. The A1 antenna occupies one full side panel and views in a direction 120° from the other antennas. The Electronics Unit and Radiometers are located inside the spacecraft radiation vault

Table 3 Nominal MWR characteristics

Channel ^a	Center freq ^b [GHz]	Center wavelength [cm]	Range ^c [K]	Bandwidth ^d [MHz]	Bandwidth ^d [%]	NEDT ^e [K/Hz ^{1/2}]	Beamwidth [deg]
1hi	0.600	50	0–1000	21	3.50	0.187	20.6°
1lo			0–10000				
2hi	1.248	24	0–800	43.75	3.51	0.171	21.0°
2lo			0–8000				
3	2.597	11.55	0–700	84.5	3.25	0.133	12.1°
4	5.215	5.75	0–600	169	3.24	0.123	12.1°
5	10.004	3.0	0–400	325	3.25	0.066	12.0°
6	21.900	1.37	0–300	770	3.52	0.060	10.8°

^aChannels 1 and 2 have high (hi) and low (lo) gain outputs to accommodate atmospheric and synchrotron emissions respectively. The upper end of the dynamic range specification for each channel was set to be at least two times the expected maximum antenna temperature from either

^bBandpass center at 300 K

^cThe antenna temperature range in which the receiver outputs are linear

^dNet noise-equivalent bandwidth

^eNoise equivalent ΔT (net $1-\sigma$ uncertainty in a 1-s integration due to inherent receiver white noise)

out-of-band signal rejection. The 4% width of the RF passband was driven by the capability of the inherently narrowband patch and slotted waveguide antennas used for channels 1 through 5. The RF signal is converted directly (i.e., without frequency down-conversion) to DC by a diode detector, which is then followed by a video amplification. The signal is



Fig. 7 The MWR Instrument in its flight configuration. The MWR was assembled on a spacecraft mockup frame in May 2010 for end-to-end testing just prior to delivery for spacecraft integration. A. View of the assembled instrument from the A1 antenna side. Left to right, J. Oswald, M. Janssen, and S. Brown. B. The Electronics unit (*upper left*) and Receiver unit (*lower right*). C. View of the assembled instrument from the A2–A6 antenna side

then converted to a train of pulses by a voltage-to-frequency converter. The thus-digitized signal is then read-out, packaged, and sent to the spacecraft computer system by the MWR Electronics Unit. The six receivers R1–R6 of the MWR instrument are bolted together to form a single compact unit (see Fig. 7B)

Three noise diodes with brightness temperatures in the range 100–300 K are placed strategically in the receivers' front-ends for both gain calibration and diagnostic purposes: one between the antenna and the Dicke switch, one between the Dicke switch and an isolator, and the last between the isolator and the first low-noise amplifier (LNA). The two lowest frequency receivers have two output channels each, one at low gain and one at high gain, to accommodate the large dynamic range required to observe Jupiter's synchrotron emission at the respective frequencies. The isolator is a ferromagnetic device, the characteristics of which are susceptible to the direction and strength of a magnetic field. Hence they are enclosed in mu-metal to shield them from Jupiter's strong field.

Up to five low-noise amplifiers (LNAs) are chained in each receiver to provide sufficient gain for the detector, typically about 55 dB total gain. Attenuators are used between the amplifier stages to optimize matching and suppress interaction between the gain stages, as well as to allow flexibility during the build to fine tune the gain setting. Low noise figure, high

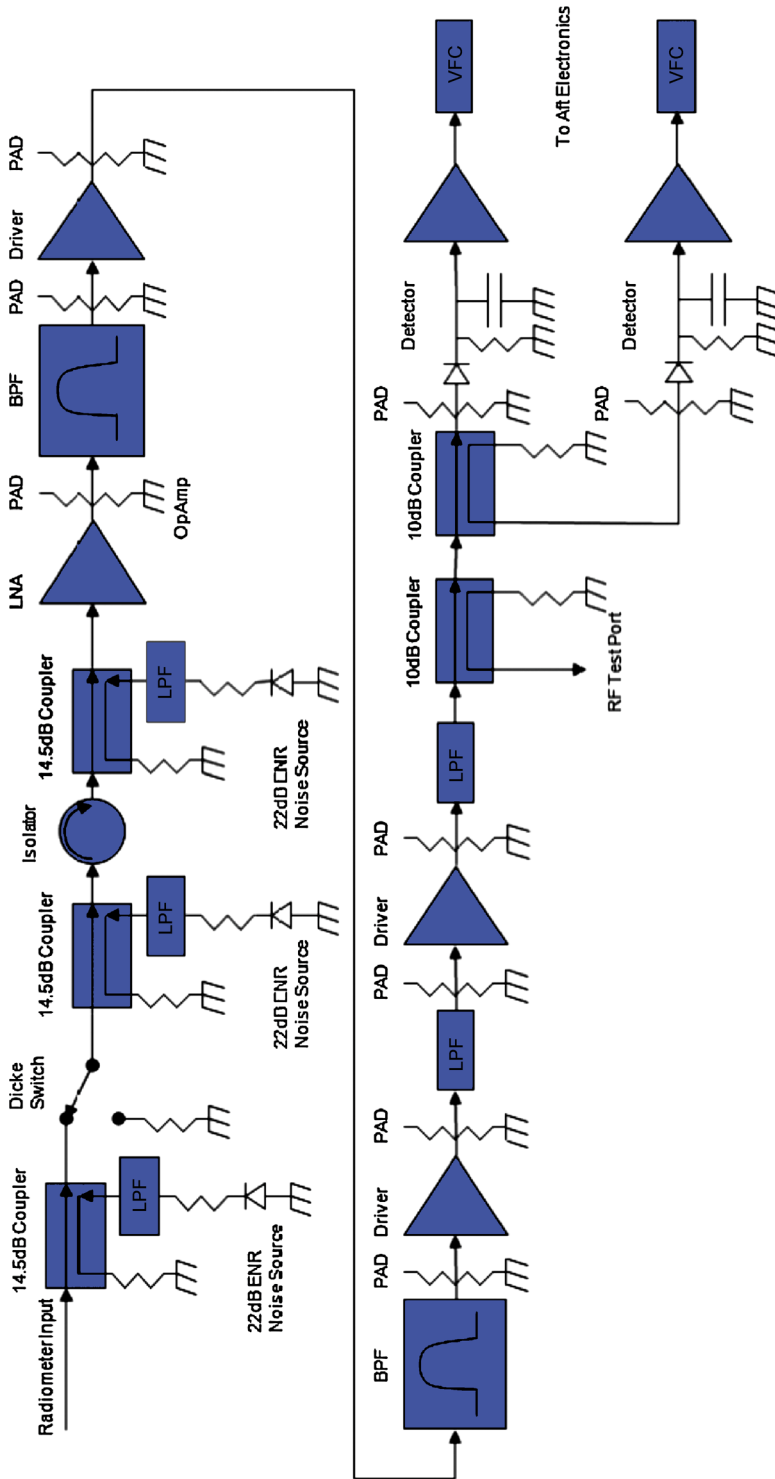


Fig. 8 Receiver block diagram. R1 and R2 circuits are shown. R3 through R6 are the same except without the extra detector and output

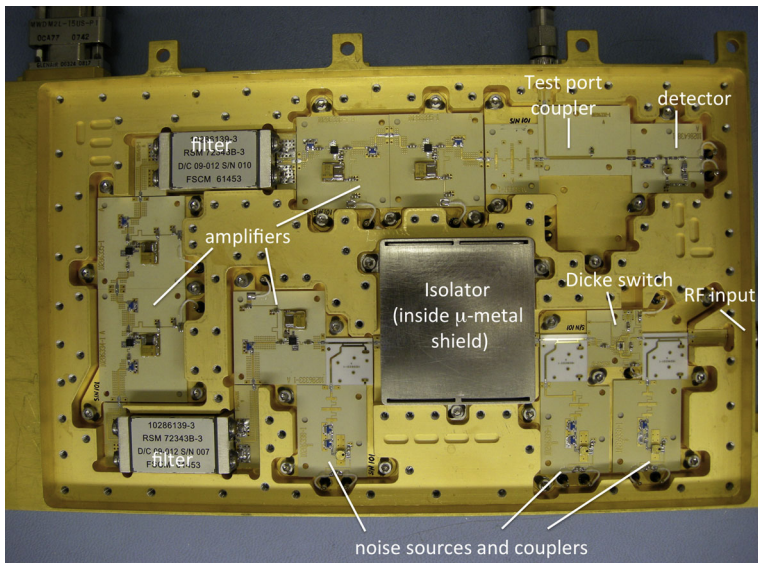


Fig. 9 Receiver R3 shown from RF side with cover removed. The output of the detector feeds through the baseplate to the digital section of the receiver. The filters shown are narrow bandpass filters. The overall box dimension is $130 \times 250 \times 31$ mm

gain, and good stability in addition to low power consumption were all important factors in selecting the amplifiers. An LNA bias circuit was designed with built-in temperature compensation reducing the receiver gain over temperature to less than 0.1 dB/C for all receivers throughout their temperature operating range of -15°C to $+30^{\circ}\text{C}$.

Although we use a common design, each receiver is unique in that they require components suitable to their respective frequencies along with modifications in the circuitry to accommodate them.

4.1.2 Electronics Subsystem

The electronics unit (EU) consists of a dual redundant Power Distribution Unit (PDU), a single string Command and Data Unit (CDU), a Housekeeping Data Unit (HKU), each of these built as “slices” for assembly into the box-shaped unit comprising the EU (see Fig. 7B). The PDU has two slices: (1) the PDU-R, which provides power distribution to the receivers, and (2) the PDU-D, which distributes power to the “digital”, or other EU slices. The CDU is a single slice. The HKU comprises two identical slices, HKU1 & HKU2.

The PDU converts the 28 V power from the spacecraft into DC voltages used to power the various digital and RF circuits of the MWR. A $+5$ V output powers the CDU, a ± 15 V output powers the HKU, while the receivers use ± 12 V, $+7$ V, -5 V, and $+15$ V outputs.

The CDU is an 8051 microcontroller-based system that includes circuitry, logic and software to (1) service and execute spacecraft commands and telemetry, (2) retrieve, integrate, assemble and control MWR science and housekeeping data, and (3) interface to ground support equipment (GSE) for control, command and telemetry functions. The CDU also has an FPGA that integrates CDU sub-module functions. Spacecraft communication with the CDU is through dual, redundant RS-422 interfaces with a transfer rate of 57.6 Kbps. Two FIFOs buffer incoming and outgoing data. Flight software developed for the 8051 microcontroller

is burned into a PROM, while patches may be uploaded through the spacecraft interface. All of the FPGA and 8051 clocking is derived from a master crystal oscillator contained in the unit.

The CDU includes circuitry and logic to interface with two separate housekeeping voltage-to-frequency converters (VFCs) and the receiver VFCs. Counters are implemented inside the FPGA and mapped into 8051 memory space. The CDU also includes a Dicke-switch control signal, six RF control signals to turn the LNAs in the receivers on or off, and three noise diode control signals. A single control signal is used to control the Dicke switches in all six receivers simultaneously, while each noise diode control signal turns on the corresponding noise diode in each receiver. All of these signals are optically isolated, can be set through FPGA registers, and mapped into 8051 memory space.

The housekeeping units HKU1 and HKU2 acquire temperature measurements for radiometric calibration and instrument health monitoring, and voltage measurements for PDU health monitoring. There are a total of 128 multiplexed channels (64 per HKU) with 112 allocated to temperatures and 16 to voltages (including calibration channels). Because of the radiation environment and predicted sensor temperature ranges, thermistors are used for temperature measurements within the vault while platinum resistive thermometers (PRTs) are used for external temperature measurements. The instrument was designed for a total ionizing dose of 6krad inside the vault and 1Mrad outside the vault. The CDU selects the temperature channel via HKU multiplexer addressing.

4.1.3 Antennas

The concurrent needs for narrow beamwidths, low sidelobes, and well-measured gain patterns provided stringent antenna design requirements unique for the MWR instrument. The achievement of narrow beamwidth is strongly constrained by considerations of size and mass at the lowest frequencies because of its inverse relationship to aperture size and the limited available space on the spacecraft. Nevertheless, the low periapse of the Juno orbit allows sufficient spatial resolution to be obtained on Jupiter with a modest but achievable beam size of 20° . The diminishing constraints with increasing frequency allowed us to achieve a 12° beamwidth at the third lowest frequency with a more modest impact on spacecraft design, which we then employed in the remaining antennas. Each antenna was designed to match its respective receiver in bandpass and out-of-band signal suppression, which was verified after the subsystems were built and tested.

Table 4 summarizes the characteristics of the antennas. Three separate design approaches were found to be optimum at the different MWR frequencies. The least mass per unit area is achieved by a patch array design, where a well-designed 5-by-5 array was found sufficient to achieve a 20° beamwidth with acceptable sidelobe performance (Chamberlain et al. 2010). The A1 antenna is seen in Fig. 7A, and consists of 25 patch elements in a 5-by-5 square grid with >0.5 wavelength element spacing, attached to the top (ground plane) side of an aluminum honeycomb panel. The A2 antenna (lower antenna in Fig. 7C) is a scaled version of the A1 antenna. The patch elements are fed through a corporate feed network of power dividers and copper/SiO₂ coaxial cables (described further below) attached to the bottom side of the panel. The feed network approximates a separable Taylor distribution with -30dB sidelobes, and was optimized to minimize the overall antenna sidelobes. The main beam efficiency (defined as the power within 2.5 times the half-power beamwidth) for all the antennas is 99% or greater, meaning only 1% of the power received originates from the sidelobe region. Normally patch antennas use a dielectric material to separate the radiating element from the ground plane; however, the electron flux encountered during a Jupiter

Table 4 Antenna characteristics

Antenna	Nominal center frequency [GHz]	Bandwidth ^a [%]	Beamwidth ^b [deg]	Design	Dimensions $L \times W \times D$ [cm]	Mass [kg]
A1	0.6	5.0	20.6	5 × 5 patch array	160 × 160 × 13.1	13.83
A2	1.25	5.0	21.0	5 × 5 patch array	76.8 × 76.8 × 9.8	4.89
A3	2.6	4.6	12.1	8 × 8 slot array	77.1 × 67.3 × 8.9	7.25
A4	5.2	6.0	12.1	8 × 8 slot array	38.6 × 34.0 × 5.7	1.46
A5	10.0	4.6	12.0	8 × 8 slot array	20.1 × 17.9 × 4.4	0.51
A6	22.0	>5	10.8	Corrugated horn	15.3 × 15.3 × 34	0.75

^aMeets all requirements over this range around the center frequency

^bHalf-power beamwidth averaged over bandwidth

perijove pass by the antennas was anticipated to deposit an amount of charge that would cause an unacceptable level of arc discharging. We therefore avoided the use of dielectrics in the patch support structure, instead supporting each patch by a centered cylindrical metal pedestal attached to the antenna ground plane by surface-mount studs and fasteners. Each antenna element was machined from a monolithic block of aluminum to give it structural integrity. The support provides DC coupling to ground, this position being a zero-field point in the patch radiation field. Cantilevering spines on the tops of the patches made them rigid and capable of meeting vibration requirements. In addition the off-center feeds attach electrically to the patches via a sliding contact that allows movement of each patch relative to the ground plane, making this contact invulnerable to vibration.

A slotted array antenna design was used for antennas A3 through A5 using a similar slot amplitude taper. Although intrinsically more massive than a patch array design, the smaller size of these antennas allows the use of a conventional slot array design to achieve higher spatial resolution and low sidelobes without paying a severe mass penalty. The A3 and A4 antennas are assembled onto a common mounting frame on a second spacecraft side, above the A2 antenna (see Fig. 7C). The mechanical interface to the spacecraft is a set of bosses located on the mounting frame, which are used to attach it to the spacecraft. The A3 and A4 electrical interfaces are through a coaxial connection, while the A5 electrical interface is through a WR-90 waveguide. The A5 antenna is attached to a bracket on the top of the spacecraft. Corrugated horns provide superior beam patterns at the cost of relatively high mass, this being an acceptable penalty at our highest frequency. The A6 antenna is a corrugated horn with a profiled shape to minimize size and mass while at the same time providing the desired beamwidth with extremely low sidelobes. It is mounted on the top panel of the spacecraft (next to the A5 antenna as seen in Fig. 7C) and is fed by a WR-42 waveguide.

Two sets of transmission lines, one external to the vault and one internal, carry the signals from the antennas along the body of the spacecraft to the receivers in the vault, using a feedthrough in the vault wall. These lines vary in length from about 1 to 3 m and produce significant attenuation (and consequently thermal reemission). They are consequently well instrumented with sensors to monitor their temperature distribution. The measured temperatures are incorporated into the calibration algorithm, using a thermal model of the transmission line to ensure fidelity. For channels 1–4, coaxial cables consisting of a copper inner and outer conductor separated by a SiO₂ dielectric are used for both the internal and external transmission lines. For channel 5, the same coaxial cable type was used from the vault

bulkhead to the receiver and WR-90 waveguide was used from the antenna to the bulkhead to reduce loss. For channel 6, WR-42 waveguide is used to connect the horn to the receiver through the vault wall. The SiO₂ dielectric cables were selected for their phase stability over temperature and lack of hysteresis often encountered with Teflon cables.

4.2 Operational Approach

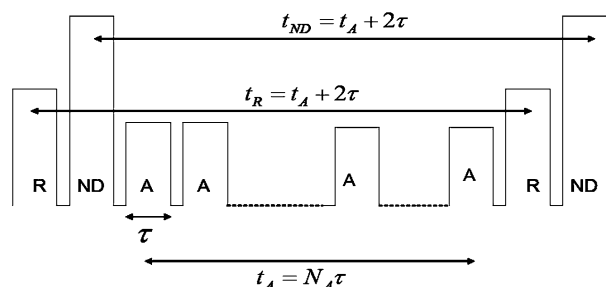
During operation the receivers accumulate integrations of the input noise power in 100-ms intervals, during which the output of each receiver's voltage-to-frequency converter is accumulated for 99 ms and read out as raw counts in the next 1 ms. The 100-ms integration interval is fixed and not adjustable. During the integration the receivers are switched to either the input from the antenna (i.e., the sky) or the internal reference load, and the noise diodes are either powered on or off. Only one noise diode can be on at a time, or all can be off. Eight switch setting states are possible for the receivers: with the Dicke switch set to either the sky or internal load, either one of the three noise diodes can be on, or all off. Switching occurs during the 1 ms read-out interval, and all receivers are switched identically; i.e., when a given switch is set for one receiver, the same setting is used for that switch on all receivers.

Figure 10 shows a typical switching sequence, where $\tau = 100$ ms and the cycle repeats in a time $t_A + 2\tau$. The sequence length is effectively arbitrary and can be set by uplink if desired. Twenty-two preset sequences are contained in ROM and can be selected by uplink command, although testing during cruise showed that only two sequences were needed in orbital operations.

The sequence used for full data rate output repeats after sixty 100-ms integrations, or 6 s, during which the sky is observed with noise diodes off fifty times (83% duty cycle on the sky), the reference load is observed five times, and one of the noise diodes is observed five times (three with the Dicke switch set to the sky and two set to the reference load). In ground science data processing, a running average with an adjustable window is performed on noise diode and reference load measurements to reduce the noise on the antenna measurements. This sequence allows the sky signal to be fully sampled at the 2 rpm spin rate of the spacecraft, which rotates 1.2° each 100 ms integration (1/10 of a beamwidth at our smallest beamwidth), while collecting sufficient data on load and noise diode signals to stabilize the gain variations that occur on much longer time scales.

The full data rate is obtained when all integrations are collected and sent to the ground. However, there are times when the full data rate is not necessary while overall data volume is a concern for operations, such as long periods away from perijove when the zero-level baseline reference needs to be tracked but only a minimal amount of data is needed. In this case we can exercise a software option to send only a commanded fraction of the integrations to the ground without otherwise altering the hardware functioning, thus resulting in minimum impact to both the hardware and ease of operation.

Fig. 10 Nominal switching sequence



5 Instrument Calibration and Error Analysis

The success of the MWR experiment depends on our ability to meet the requirements set in Sect. 3.3. The calibration approach we use and its associated error model are new and challenging. We outline this approach here. In brief, the quality of our calibration depends on our ability to account for all factors that contribute to errors in the determination of the limb-darkening parameter R . This has two aspects: the antenna temperature calibration, or the relative and absolute calibration of the received power, discussed in Sect. 5.1; and the antenna pattern correction discussed in Sect. 5.2 that allows us to relate this power to the source brightness temperature distribution.

The final calibration depends on a combination of pre- and post-launch efforts. The pre-launch calibration strategy involved testing at the sub-system, system and spacecraft levels to determine a set of calibration coefficients defined in an instrument model, and to characterize system stability to ensure that the error budget is met. After delivery of the instrument for integration into the spacecraft, we used the final results from these tests to produce a prelaunch estimate of the net error. That estimate is presented in this section, and a post-launch effort for verification and improvement of this model will use flight data is described in Sect. 6.

5.1 Receivers

The antenna temperature (T_a) represents the power collected by the antenna that enters the receiver; i.e.,

$$T_a(\theta, \phi) = \int_0^{2\pi} \int_0^\pi T_b(\theta', \phi') G(\theta' - \theta, \phi' - \phi) \sin \theta' d\theta' d\phi' \quad (4)$$

where $T_b(\theta', \phi')$ is the brightness temperature in the direction of the solid angle element $\sin \theta' d\theta' d\phi'$ and $G(\theta' - \theta, \phi' - \phi)$ is the gain of the antenna in this direction for an antenna pointed in the direction (θ, ϕ) . The gain pattern is normalized so that

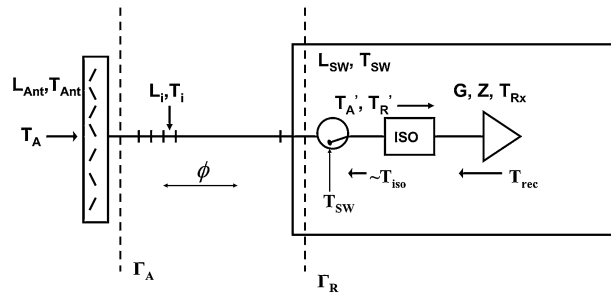
$$\int_0^{2\pi} \int_0^\pi G(\theta, \phi) \sin \theta d\theta d\phi = 1 \quad (5)$$

The receiver calibration must accomplish two objectives: it must convert the raw count output from the receiver detectors to units of brightness temperature in Kelvin, and it must account for variations in this output with time. The former, the absolute calibration, is ultimately achieved by the use of hot and cold reference targets observed through the antenna. The relative calibration depends on knowing how the absolute calibration depends on all observational conditions of the instrument. Both depend on a detailed knowledge of the characteristics of the instrument that affect its time dependence.

5.1.1 Instrument Model

The instrument model is depicted in Fig. 11. It was developed to relate the antenna temperature of each radiometer to raw radiometer counts through the entire system. From the left of the figure to the right are, respectively, the antenna, the RF transmission line, the radiometer input, the Dicke switch and load, and the isolator, followed by the first LNA and the rest of the radiometer back end. The model includes the distributed loss along the front end from the antenna and transmission lines, along with their corresponding self-emission. It includes two arbitrary reflection planes, one behind the antenna and one at the input to the radiometer.

Fig. 11 MWR instrument model diagram



A standing wave is anticipated between these two planes that can be modulated by the phase length between them. In operation the gains of the MWR receivers are calibrated by periodically injecting an additive noise signal from a noise diode as illustrated in the switching diagram of Fig. 10.

In the model we write the raw count output of the radiometer for each position of the Dicke switch in terms of the various model parameters including the losses and physical temperatures of its components and the internal gain. We subtract these and solve for the antenna temperature, in the form

$$T_a = \frac{C_a - C_r}{C_{sys}} + T_{offset} \tag{6}$$

where C_a is the raw-count output in the antenna position, C_r is the raw-count output in the reference load position, T_{offset} is the Dicke load referenced to the antenna input, and G_{sys} is the system gain, of the form

$$G_{sys} = G_r f(\Gamma_i, L_i, T_i) \tag{7}$$

where G_r is the receiver gain referenced to the Dicke reference plane (just before the isolator). Both G_{sys} and T_{offset} may be described in terms of specific model parameters that include the reflections Γ , ohmic losses L and physical temperatures T of all contributing elements in the signal path from the antenna to the receiver amplifier. Our detailed model for each receiver contains 35 such independently adjustable parameters. The noise diodes are used to track the system gain G_{sys} , e.g.,

$$G_{sys} = \frac{C_{nd+a} - C_a}{T_{nda}}, \quad G_{sys} = \frac{C_{nd+r} - C_r}{T_{ndr}} \tag{8}$$

where T_{nda} and T_{ndr} are the noise diode brightness referenced to the input of the antenna when they are fired in the antenna and reference positions respectively. The redundancy in both diodes and switch setting provides diagnostic information while guarding against the failure of a single noise diode. The noise diode brightnesses are calibrated pre- and post-launch against known sources as described in the next section. They are not assumed to be stable over time and brightness variations are tracked relative to the sky background during cruise (Brown et al. 2007).

5.1.2 Pre-Launch Antenna Temperature Calibration

The calibration consisted of the determination of all of the parameters of the model, for each receiver, ultimately relating them to an absolute gain determination using hot and cold reference targets observed through the antenna. Testing was done at both the component

level and at various levels of system integration, culminating with an end-to-end test of the entire system on the spacecraft.

Two of the key system-level tests were the instrument thermal-vacuum (TVAC) test and the calibration end-to-end test. In the TVAC test, the entire system, with the exception of the antennas, was mounted in a flight like configuration and thermal controllers were used to vary the temperature of the instrument front end. The instrument temperature was controlled at the receiver vault wall interface and at the antenna end of the radiofrequency transmission line (RFTL) connecting them. In this way, variable thermal gradients could be introduced along the radiometer front end. A microwave calibration system (MCS), developed by the University of Michigan, was used as a stable calibration source and was connected in place of the antenna (Peng et al. 2007). The MCS consisted of a temperature stabilized active cold load (Weatherspoon and Dunleavy 2006; Sobjaerg et al. 2009) with an effective brightness at the MCS output near 100 K, an ambient reference load near 300 K and a noise diode that provided ~ 100 K of additional noise on top of either source, giving four stable calibration points between about 100–400 K. The MCS was switched between these four states once per second. A stainless steel transmission line was used to connect the MCS to the MWR to decouple the instrument temperature variations from the MCS. The TVAC data were used to find the final pre-launch antenna temperature calibration coefficients needed for Eqs. (6) and (8). The MWR component level measurements were used as a first guess and tuned, within the component measurement uncertainty, to minimize the RMS difference between the MCS antenna temperatures and the MWR calibrated antenna temperatures. The emission contribution from the stainless steel thermal break had to be accounted for in the processing and was one of the larger sources of uncertainty in the derived calibration coefficients. The antenna loss over temperature was measured in a separate test.

A calibration end-to-end test was performed to verify the calibration of the final integrated system with the antennas. A large 2×2 m temperature controllable blackbody calibration target was constructed. The target was made out of porous pyramidal microwave absorber like that typically found in an anechoic chamber. Heated air was force through the foam that allowed it to be controlled over the range of ambient (~ 293 K) to 338 K. Twenty-four temperature sensors were used to measure its mean temperature at a given setpoint, and spatial differences across the target were typically less than 2K. The MWR system gain at ambient instrument temperature, which includes the transmission through the antenna and RFTL, was verified by comparing the MWR calibrated antenna temperature to the target temperature as the target was stepped in increments of 10 K from 393–338 K. If we conservatively estimate the error in our knowledge of the target temperature to be 1.5 K at the warm end, then the absolute calibration at ambient is verified with an uncertainty of about 2%.

5.2 Antennas

The objective of the antenna design and pattern characterization was to obtain the best possible spatial resolution on Jupiter while fully accounting for off-axis signals, thereby enabling the best estimate of the limb-darkening parameter R in any given antenna footprint. The uncertainty in our determination of R having to do with the antennas depends on several factors: (1) antenna beam sidelobe levels, (2) how well we know them, and (3) the observational geometry and the global brightness distribution on the sky from the perspective of the spacecraft, as described in this section. Our approach was first to minimize the beamwidth and sidelobes of all the antennas by design as constrained by mass, size, and environmental limitations imposed by the spacecraft and mission design. An antenna pattern error model

was developed to set performance requirements on the antennas, allowing us to make initial allocations for sidelobe levels and knowledge required of them. After building the antennas we measured their patterns over the full sphere using state-of-the-art techniques at each frequency. At the same time we performed studies that enabled us to estimate the uncertainties in the pattern measurements. The detailed antenna subsystem error budget was iterated and rebalanced as we made progress with our development and better understood the uncertainties. We finally determined the best estimate of the uncertainties in R for the antenna pattern error model error prior to delivery for spacecraft integration.

5.2.1 Antenna Pattern Correction (APC)

The measured antenna temperature T_a is related to the source brightness temperature distribution T_b as an integral of this distribution over the antenna gain pattern as described by Eq. (4). What we want ideally is the source brightness distribution T_b obtained by the inversion of this equation. The process to achieve this inversion is often called an “antenna pattern correction”. Ultimately this is constrained by the finite beamwidth of the antenna; nevertheless, we wish to obtain a result that is independent of features of the measurement system, such as contributions entering through antenna sidelobes. In our case we wish to obtain the unbiased brightness temperature of any point in Jupiter’s atmosphere as seen from a specific emission angle and limited only by the antenna resolution. Every observation is not only contaminated by sidelobe contributions but is averaged over a range of emission angles and hence biased by the curvature of the atmosphere. Both must be accounted for. We have found it convenient to divide this problem into two parts. In this section we deal with the removal of sidelobe contributions, and account for the emission angle biasing in a later section. To begin let us consider the average brightness in the main beam of the antenna. Rewrite the antenna gain pattern as the sum of a main beam and a sidelobe pattern respectively, namely

$$G(\theta, \phi) = G_{mb}(\theta, \phi) + G_{sl}(\theta, \phi) \quad (9)$$

where the integral of $G(\theta, \phi)$ over the sky is normalized to unity as in Eq. (5). The central lobes of the MWR antennas are well approximated by Gaussian distributions with the half-power beamwidths given in Table 3. Let us define the main beam pattern G_{mb} to be such a Gaussian. If the gain pattern $G(\theta, \phi)$ is known, then the sidelobe pattern is determined from the measured gain pattern $G(\theta, \phi)$ as

$$G_{sl}(\theta, \phi) = G(\theta, \phi) - G_{mb}(\theta, \phi) \quad (10)$$

We may write the average brightness in the Gaussian main beam as

$$\bar{T}_{mb} = \int_0^{2\pi} \int_0^\pi T_b(\theta', \phi') G_{mb}(\theta' - \theta, \phi' - \phi) \sin \theta' d\theta' d\phi' / (1 - b) \quad (11)$$

where

$$b = \int_0^{2\pi} \int_0^\pi G_{sl}(\theta, \phi) \sin \theta d\theta d\phi \quad (12)$$

Equation (4) may then be solved to find the resolution-limited scene brightness temperature

$$\bar{T}_{mb}(\theta, \phi) = \frac{1}{1 - b} \left[T_a(\theta, \phi) - \int_0^{2\pi} \int_0^\pi T_b(\theta', \phi') G_{sl}(\theta' - \theta, \phi' - \phi) \sin \theta' d\theta' d\phi' \right] \quad (13)$$

Equation (13) is an antenna pattern correction that effectively reduces the inversion of the expression for the measured antenna temperature to obtain boresight brightness temperature

to a Gaussian deconvolution. Its full solution depends on knowing the full beam pattern and the brightness distribution outside of the main beam; however, the second term in the bracket of Eq. (13) turns out to be generally small (e.g., see the discussion in the following section with regard to the effect of perturbations in the far sidelobes), and we can use a model for Jupiter's brightness distribution along with our measured gain pattern to account for it. The subsequent deconvolution to obtain boresight brightness temperatures is outlined in Sect. 7.2. Specific applications of the overall approach may evolve and are left to future papers.

5.2.2 Pattern Measurement and APC Error Analysis

Meanwhile, we turn here to the question of pattern measurement and knowledge requirements that make this approach feasible with a practical measurement system. The final far field patterns for all antennas were measured over the full sphere under contract at Nearfield Systems Inc. (NSI) in Torrance, California, using their spherical near-field chamber. The *a priori* errors were not well understood, and the effort described in the section was to obtain a conservative estimate of how they depended on gain at each frequency for use in the final error analysis. Measurements were taken throughout the passband of each receiver, with the final patterns obtained by averaging over these bandpasses. The final patterns for representative flight antennas are shown in Fig. 12. Errors in the determination of the limb-darkening parameter R through the antenna pattern correction arise from imperfect knowledge of both of these beam patterns as well as the sky brightness distribution outside of the main beam. We investigated the uncertainties in the beam pattern both by analysis and test, using multiple approaches where possible, following which we modeled the effect of the resulting beam uncertainties on the determination R .

First, a 22:1 working scale model of the A1 antenna operating at 13.3 GHz was constructed and incorporated into a mockup of the spacecraft that reproduced the features (e.g., solar panels, Waves antennas) that we thought might affect the A1 pattern (see Fig. 13). Patterns measured at a cylindrical test range at JPL with and without such features agreed within $\ll 1$ dB to levels approaching the -40 dB limit of the test range. This being the antenna most likely to be affected by near field structure, we concluded that there was no concern for the influence of the spacecraft for any of the antennas.

Five engineering model (EM) antennas were built (A1–A5) and their patterns measured, A1–A4 at NSI under contract, and A4 and A5 on a cylindrical range at JPL. An error study was performed by NSI in which their range system was evaluated and tests were included in the pattern measurement of two representative antennas (A1 and A3) to determine the possible distortions caused by range effects. On the basis of a linearity test it was concluded that any departures from linearity in the test equipment were negligible. A comparison was made of the duplicated measurements of the A4 pattern at JPL and NSI. Finally, the flight (FM) antenna patterns were measured at NSI before environmental testing, and for A2 after environmental testing. Comparisons were made between EM and FM antennas, and between the A2 antenna before and after environmental testing. All comparisons were consistent with the expected range errors.

At the same time we calculated the expected patterns using several methods, with the commercial finite element method solver HFSS used for the final calculations. The results were compared with the measured patterns, providing a strong measure of confidence in both measurements and calculations. Figure 14 shows an example in which the measured and calculated patterns for the EM A1 are successfully compared despite the existence of range reflections in the measurements. We compared the calculated and measured patterns for all

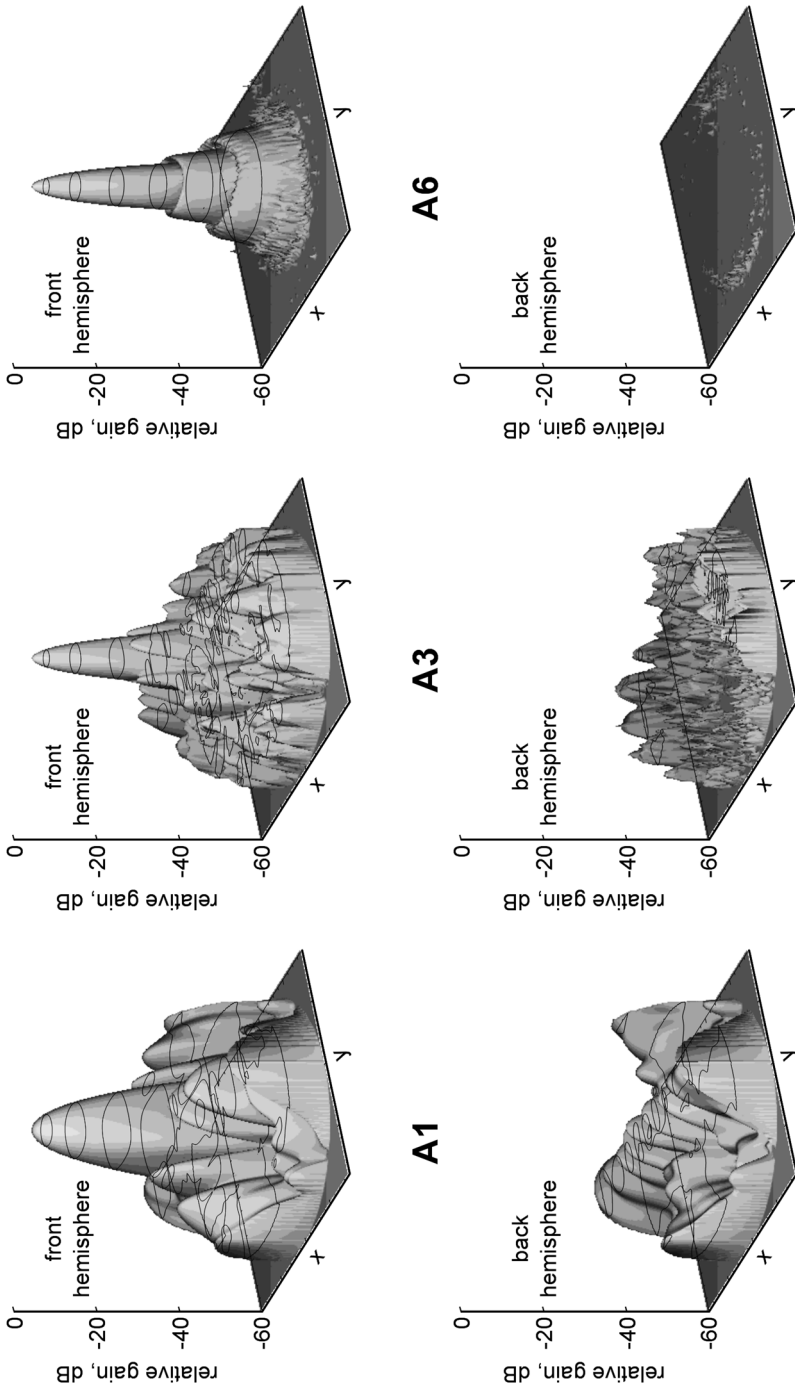


Fig. 12 Final antenna patterns after averaging across the receiver passbands, shown for both front (*top*) and back (*bottom*) hemispheres for representative antennas A1 (patch array with 20° beamwidth), A3 (slot array with 12° beamwidth), and A6 (horn with 12° beamwidth). The gain scales are logarithmic relative to the central peak with contours shown at -3, -10, -20, -30, -40, and -50 dB below the peak

Fig. 13 A functional 22:1 scale model of the A1 antenna mounted on a mockup of the Juno spacecraft for testing

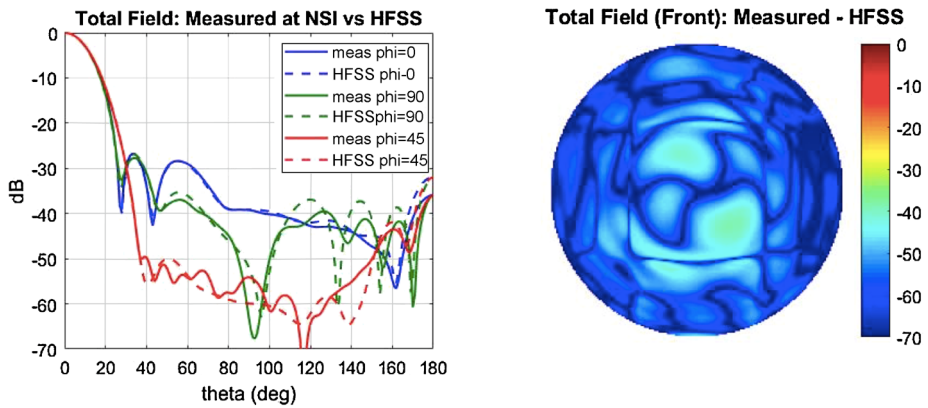


Fig. 14 Comparison of measured and computed patterns for A1. *Left:* The *dashed curves* show the principal and intercardinal pattern cuts for the A1 measured and computed patterns. *Right:* Difference in power between measured and computed patterns in the forward hemisphere, relative to the central peak power

Table 5 Final antenna pattern uncertainty estimates

	A1	A2	A3	A4	A5	A6
dB @ -30 dB	1.0	0.7	0.38	0.38	0.38	0.38
dB @ -40 dB	2.0	1.5	0.83	0.83	0.83	0.83

antennas in terms of their average sidelobes in selected annuli. The averaged measurements agree with the computed values in the front hemisphere with accuracy generally much better than 1 dB. Agreement was poorer in the back hemisphere, as might be expected because the back structure in the measurement configuration differed from the bare antenna case assumed in the HFSS calculation. Nevertheless, the deviations were at levels where the beam knowledge requirement is much more relaxed.

Consideration of all these results led to the error estimates shown in Table 5 for the general error levels in the pattern at two mean sidelobe levels. These levels were chosen to best quantify the pattern errors that contribute most to the antenna pattern correction. These values are conservative and represent what we believe to be a reasonable worst case for the analysis to obtain the APC error budget.

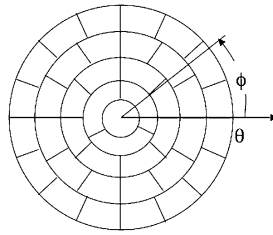


Fig. 15 Schematic illustration of segmented antenna pattern model. The pattern area is segmented into regions of size approximately equal to the main beam half-power width. A random error with a Gaussian distribution is added to the measured pattern in each segment with an amplitude consistent with a given point-to-point error model

We investigated the effect of pattern errors on the determination of the limb-darkening parameter R using a Monte Carlo approach. Let us consider an observation at some emission angle θ , and suppose that we randomly perturb a “true” antenna pattern and recompute the model antenna temperature at this angle as the “measured” value. We repeat this n times so that the measured antenna temperature T_a^m recomputed for the i th perturbation is

$$T_{ai}^m(\theta) = T_a^i(\theta) + \delta_i(\theta) \quad (14)$$

where $T_a^i(\theta)$ is the “true” antenna temperature. As discussed in the previous section, the antenna temperature T_a is closely related to the boresight brightness temperature T_b , and we use perturbations on the former as a proxy to actual brightness temperature variations for error estimation. We may then approximate the measured limb darkening parameter R_i^m for this perturbation as

$$R_i^m(\theta) = R^i(\theta) + (\delta_i(\theta) - \delta_i(0))/T_a^m(0) \quad (15)$$

where we ignore all terms of order bT_a or δ_i/T_a . We may identify

$$\Delta R_i(\theta) = (\delta_i(\theta) - \delta_i(0))/T_a^i(0) \quad (16)$$

as an error in the limb darkening measurement at the point θ . This is readily evaluated for any given perturbation, and the statistics of the ensemble over n trials allows us to estimate the net uncertainty ΔR in our determination of R . In particular we take our measured antenna pattern as the true pattern, and develop a perturbation model for the antenna pattern to reflect the level of uncertainty at each point in it. We then use this model to estimate the net error $\Delta R(\theta)$ at that point. We determine n empirically to ensure convergence to a stable value.

We used a segmented perturbation model in which the antenna pattern outside the main beam is arbitrarily subdivided into regions of the same approximate area of the main beam half-power width (i.e., 20° for A1 and A2, and 12° for A3–A6), which represents the approximate angular scale on which beam variations can occur (see Fig. 15). The Aquarius project used a similar approach to determine their antenna performance (see Wentz and Levine 2011). We randomly perturbed each of these regions with a magnitude consistent with the values given in Table 5, and also allowed for an increase in the beam diameter by 0.5%. We then calculated the rms deviation of R from its unperturbed value over an ensemble of trials for a given frequency and observing geometry. Using our JAMRT program to compute model brightness temperatures, we varied the observing geometry of range, latitude, and emission angle θ to correspond to the range of those experienced in a typical Juno orbit.

Fig. 16 Uncertainty in R vs. emission angle and latitude for representative channels as determined from a beam perturbation model and a model for Jupiter's thermal emission. Latitude is indicated by color as given in the *legend*

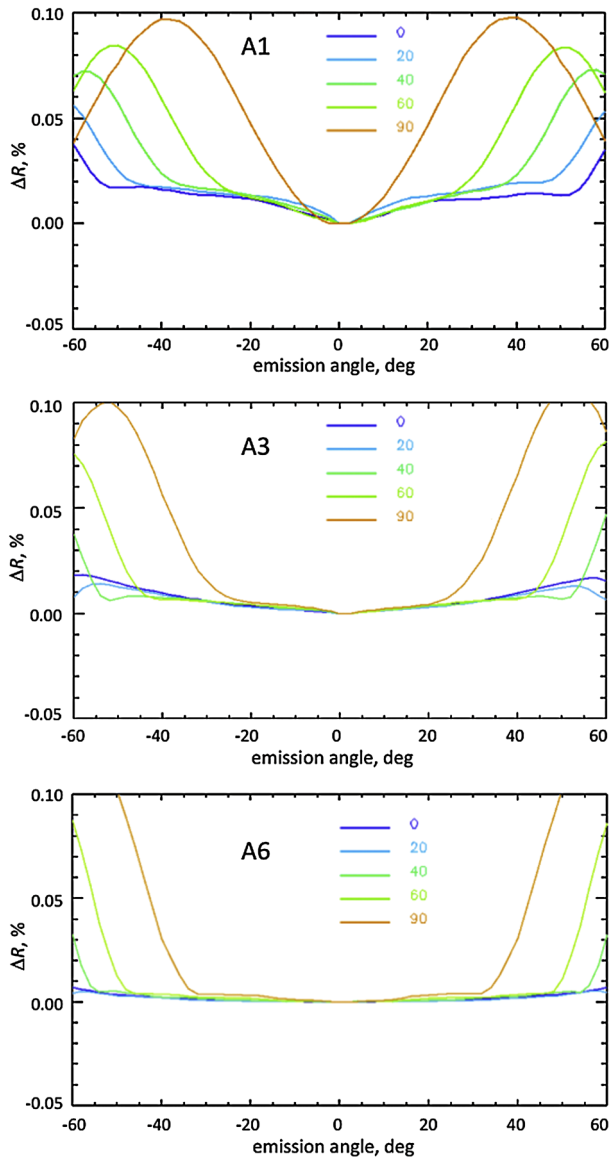


Figure 16 shows the dependence of the measurement uncertainty on beam knowledge for these observing parameters. The assumed 0.5% beamwidth increase is the dominant factor limiting the range of emission angles that are useful at a given latitude. The dependence of the uncertainty in R on latitude reflects the fact that the apparent size of Jupiter shrinks with respect to the beamwidth at latitudes away from the equator. The rapid increase in error with emission angle signifies that the main beam of the pattern has reached the limb of Jupiter and that the main beam shape becomes important. We don't take our choice of beamwidth increase seriously as a possible measurement error; instead, we consider that it provides a reasonable bound for the emission angle range that is achievable at a given latitude. Finally, we may account for uncertainties in the brightness distribution of Jupiter itself outside our

measured track by comparing the above analysis to that using an error model in which the beam is known and the uncertainties are present instead in Jupiter's brightness distribution. We note that there is no distinction between the two in Eq. (13) or in the conclusions that may be drawn. At any given wavelength we expect Jupiter's brightness to depart from that given by our nominal emission model by at most 5–10% across the disk. Since we have already considered relative sidelobe gain variations larger than this, we then conclude that this source of error is relatively insignificant.

We note that our estimates of $T_{mb}(\theta)$ are averaged over footprints that vary with θ as well for any given point in the atmosphere. Spatial brightness structure in the main beam footprints that varies as a function of the emission angle θ will lead to additional errors that must be accounted for; e.g., by using a statistical description of the structure, if known (e.g., see Janssen et al. 1995). The main beam footprint mismatch leads to a generally small uncertainty that is partially mitigated by averaging along-track nadir views to broaden the effective long dimension of the footprint to match that at emission angle θ , and by averaging out the residual error over a range of contiguous footprints. The residual error is randomly distributed and the averaging further mitigates the error. The net error is generally small if the footprints lie strictly along the sub-spacecraft track; however, the error grows if the rotation of Jupiter is not compensated and successive observations of a given point on Jupiter drift in longitude as the spacecraft moves in its orbit. This source of error in R may be almost completely eliminated by tilting the spacecraft rotation vector as described in Sect. 6.2.

Synchrotron emission enters through the far sidelobes and backlobes as we observe thermal emission from Jupiter's atmosphere. The synchrotron emission is most important at the lowest two MWR frequencies where its brightness can far exceed that of Jupiter. After careful design of the antenna sidelobes to minimize this contribution, our approach to mitigating that remaining is to model and subtract it from the measured antenna temperature. Our overall approach includes improving the model after we measure the actual synchrotron emission in orbit. We simulated observations of Jupiter here to include synchrotron emission entering through the sidelobes in order to test this approach in the face of uncertainties in the synchrotron emission modeling, thereby determining the degree of model improvement needed to meet our requirements. Using the predicted trajectory for first perijove of the mission (PJ1) to provide the observational geometry, we used our Instrument Simulator (see Sect. 7.2) to produce synthetic data for a uniform model of Jupiter's atmosphere in conjunction with models for the synchrotron emission (Santos-Costa and Bolton 2009; Adu-mitroaie et al. 2016). To estimate the error incurred by this approach, we varied the strength of the modeled synchrotron emission uniformly by 20%, a level of uncertainty we believe to be attainable once we have real data in hand, and examined the relative effect this would have on the Jupiter brightness temperature retrievals. Figure 17 shows the results as they depend on latitude and emission angle for the three most affected MWR frequencies. The gray scale contour map shows the relative difference in brightness, which we define as the Jupiter brightness with the nominal synchrotron model minus the brightness obtained with that model reduced by 20%, all normalized by the total brightness of Jupiter as a function of latitude and emission angle. This then gives a conservative estimate of the error that would result in the limb darkening, where we wish to keep the threshold below 0.1%. Positive emission angle as used here refers to the first look at a given sub-spacecraft point (the "fore" look), while negative emission angle refers to the "aft" look, obtained as the spacecraft looks backwards after it passes over the point. The asymmetry between for and aft looks is caused by the difference in range between the two. The magnitude of the difference is generally much less than a part in 10^3 (0.1%) over a wide range in emission angle. The main lobe of the antenna impinging on the limb of the planet where it directly encounters the synchrotron signal causes the sudden rise in the difference.

Fig. 17 Estimate of the error in retrieved T_b incurred by uncertainty in the knowledge of the synchrotron emission. Shown is the relative difference (i.e., difference normalized by the unperturbed brightness) obtained in a synthetic retrieval of T_b when a nominal synchrotron emission model is varied by 20%. The geometry of the Juno perijove pass of 27 Aug 2016 was used for the synthesis of time-ordered data

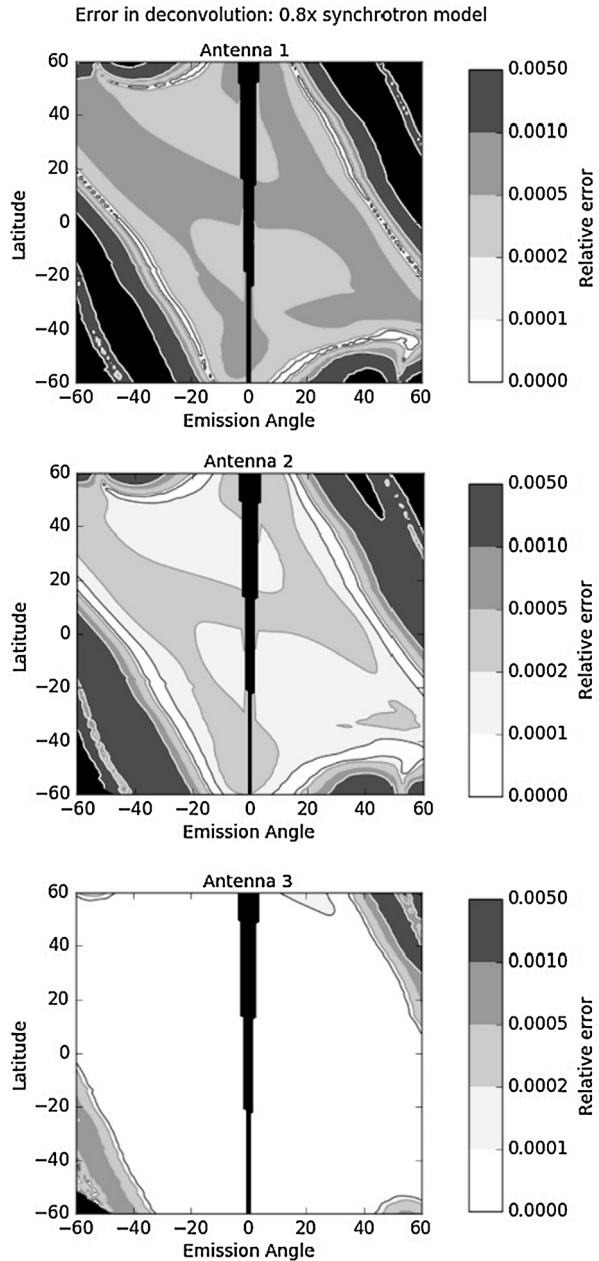


Table 6 compares the final APC prelaunch error estimates based on pre-launch measurements to our original design allocations. The breakdown for the thermal component is based on the results for the antenna perturbation model shown in Fig. 15 over the range of latitudes specified in the second requirement stated in Sect. 3.3, while that for the non-thermal (synchrotron) component is conservative and based on the calculation illustrated in Fig. 17.

Table 6 Final APC error budget in the determination of R

	A1	A2	A3	A4	A5	A6
Thermal allocation	0.06	0.07	0.06	0.06	0.06	0.05
Non-thermal allocation	0.05	0.03	0.00	0.00	0.00	0.00
Design APC allocation	0.075	0.075	0.06	0.06	0.06	0.05
Prelaunch thermal estimate	0.045	0.04	0.01	0.01	0.008	0.003
Prelaunch non-thermal estimate	0.05	0.03	0.00	0.00	0.00	0.00
Net APC current best estimate	0.07	0.05	0.01	0.01	0.008	0.003

Table 7 Instrument limb-darkening error breakdown based on prelaunch calibrations

	Ch1	Ch2	Ch3	Ch4	Ch5	Ch6
Measurement noise (5 s avg.)	0.031	0.027	0.026	0.032	0.023	0.029
Antenna temperature calibration (ATC)	0.054	0.054	0.042	0.063	0.069	0.075
Antenna pattern correction (APC)	0.070	0.050	0.010	0.010	0.008	0.003
Net error in R (%)	0.094	0.078	0.050	0.071	0.073	0.081

5.3 Prelaunch Error Budget

The final prelaunch estimate of errors in the measurement of the limb-darkening parameter R is given in Table 7 based on results described in this section. These values compare well with the initial error budget allocations in Table 2. The overall improvement in net error is primarily due to better antenna performance than expected, reflecting our initial concern on this more unproven area of our instrument design and our initial conservatism in its implementation.

We caution that these errors are based on systematic errors estimated on the basis of instrument performance only and do not include effects caused by variable observational geometries and currently unknown statistics of spatial brightness structure on Jupiter, which are discussed in Sect. 6.2.

6 Flight Operations

6.1 Cruise and Flight Calibration

The Juno cruise phase of operations consisted of a two-year inner cruise phase, an Earth flyby, and a subsequent three-year coast to Jupiter (the outer cruise). The focus of MWR flight operations during cruise was the refinement of the ground-based calibrations. The flight calibration had several objectives:

6.1.1 Establishment of a Zero-Level Baseline for Jupiter Observations

Brightness temperatures of Jupiter are measured relative to the sky, and must take into account the brightness temperature of the sky in every direction observed during Jupiter perijove. The base brightness is the Cosmic Microwave Background, approximately 2.7 K, to

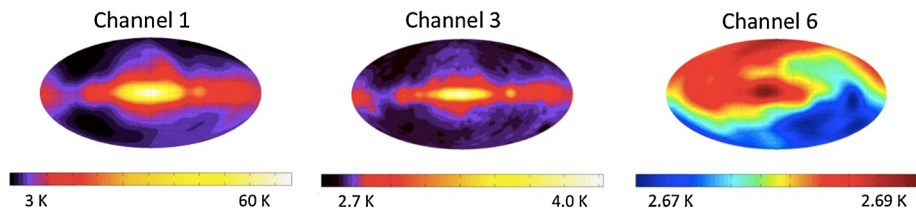


Fig. 18 All sky maps were obtained during the cruise phase to provide a brightness temperature calibration reference for operations at Jupiter. Representative maps are shown for channels 1, 3, and 6. Apart from the cosmic background emission, the dominant features in the sky in these maps are due to synchrotron emission from very high-energy electrons in our galaxy, hence galactic coordinates are used in the figures. The magnitude of the sky emission variability decreases rapidly with frequency from as high as 60 K in channel 1 to 20 mK in channel 6, where we see the ± 3 mK CMB dipole (Lineweaver et al. 1996)

which must be added the contribution from foreground sources. Discrete sources are highly diluted by the broad beamwidths of the MWR antennas; however, the distributed emissions due to energetic electrons circulating in interstellar magnetic fields within the galaxy can contribute significantly, particularly at the lowest MWR wavelength, where the brightness can be as high as 60 K in the direction of the galactic center. The MWR remained turned on during most of the inner cruise as the spacecraft spin vector slowly precessed through 180° in the Ecliptic plane (in the outer cruise the sampling was more erratic but allowed some gaps to be filled in). The final sky maps we obtained using data from inner and outer cruise are shown in Fig. 18.

6.1.2 Improvement of the Absolute Calibration Obtained from End-to-End Testing

The prelaunch end-to-end calibration used a large temperature-stabilized load covering the antennas to obtain an ambient brightness temperature reference for all of the radiometers as described in Sect. 5.1.2. The MWR instrument model and detailed component characteristic measurements in thermal vacuum were then used to establish the gain calibration with respect to that reference, valid under ambient conditions. After launch, the view of space offered a cold reference impractical to achieve on the ground. The extrapolation from ambient using the prelaunch calibration gave the correct result for the observed cold sky to within 2%, validating the absolute calibration to this level. The calibration scale was then adjusted to give the correct sky temperature at the start of the cruise.

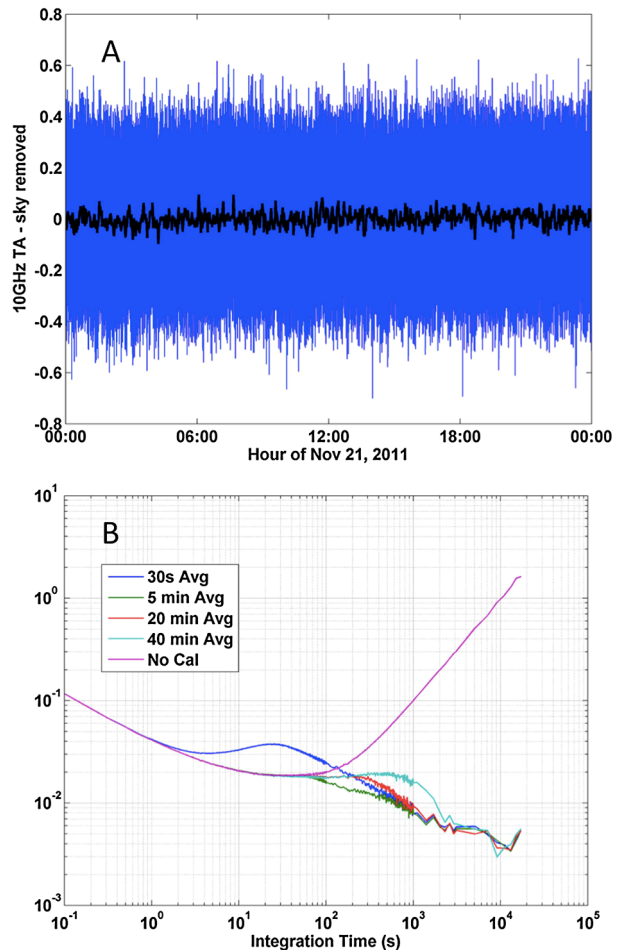
6.1.3 Refinement of the Temperature Coefficients in the Instrument Model

The temperature distribution throughout the instrument varies as the sun distance changes during cruise. As sky observations accumulated for the varying instrument temperature profile, we adjusted our instrument model temperature coefficients for gain-sensitive components such as the transmission lines to maintain the correct sky temperature. This process maintains the absolute calibration from just after launch to the temperature environment in the Jupiter orbits.

6.1.4 Determination of Statistical Performance Parameters of the Radiometers

Continuous operation on the sky provides an abundance of data to enable a detailed investigation of the performance characteristics of the radiometers and a determination of the

Fig. 19 Radiometer stability for one day's operation during cruise. **(A)** Raw data with the sky signal subtracted for the 10 GHz channel. The *blue curve* shows the 100-ms data, while the *black curve* shows the running 1-min average. **(B)** Allen variance for the same data with no calibration, and after stabilization using noise diodes and Dicke load for several calibration window-averaging times



optimum approach to calibration and stabilization. After the sky signal itself is determined this can be subtracted from the data to provide the equivalent of an ideal stable load, namely the CMB at 2.7 K. Figure 19A shows a time series of continuous antenna temperature measurements with the sky signal removed for the 10 GHz channel for a 24-hour period and Fig. 19B shows the Allen variance of these data taken at full data rate for the same 24-hr period during cruise under different assumptions for a stabilization algorithm. A running average of the Dicke load offset and noise diode referenced gain was used to reduce the white noise on the calibration measurements. An optimum integration time for these calibration measurements was found by balancing the systematic noise from the receiver gain variations against the inherent white noise component of the receivers (the latter reduces as the inverse square root of the integration time while systematic errors grow in comparison). The lower-frequency receivers benefit from longer running average times compared to the higher frequency receivers, which depend on the individual receiver stabilities and their NEDT values (see Table 3). The optimum balance was found to be relatively insensitive to calibration algorithm parameters. A similar analysis will be performed on data during the apojove portion of the Jupiter orbits and the averaging window lengths will be updated as needed to maintain optimum noise performance during the orbital phase.

6.1.5 Electromagnetic and Thermal Interference

A number of tests were made during flight to test the presence and magnitude of electromagnetic interference (EMI) and thermally-induced effects that would compromise the performance of the MWR in orbital operations. These included all transmissions from all antennas on the spacecraft, and all operations of subsystems and instruments on the spacecraft. Two perijove compatibility tests were carried out during cruise with sufficient fidelity to simulate orbital operations, in addition to which special tests were carried out to test the possibility of interference due to all possible radio transmission modes anticipated for orbital passes. There was no evidence of EMI in any of these tests—the noise statistics of the time-ordered data were carefully examined through the entire period of each test to look for departures from Gaussian noise and none were seen. Thermal transients due to subsystems powering on or off prior to or during a simulated perijove pass were seen at expected levels, namely ≤ 0.5 K/hr, and well within our design requirement.

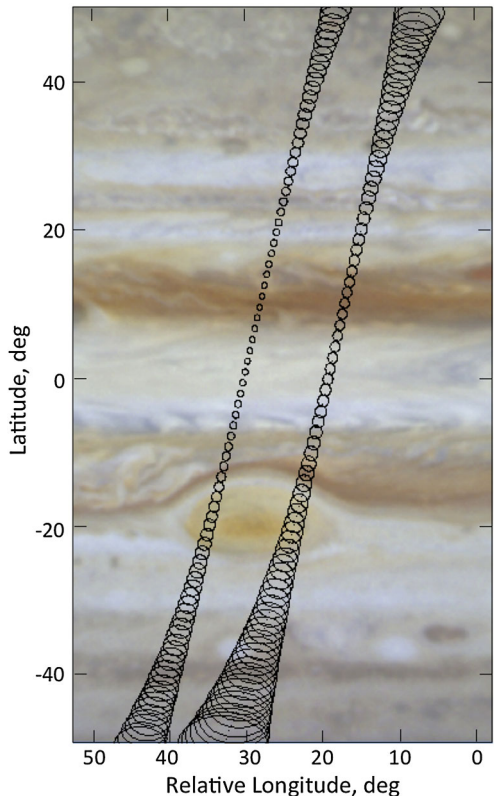
6.2 Planned Jupiter Orbital Operations

All atmospheric data is obtained during a period of approximately three hours centered on perijove. As the spacecraft moves through perijove in all orbits, each 30-s spin of the spacecraft sweeps the MWR beams through a great circle on the sky, scanning Jupiter generally along the sub-spacecraft track depending on the orientation of the spacecraft spin vector. Hence each latitude along the sub-spacecraft track is observed numerous times over a range of emission angles. Each measurement consists of a 100-ms integration of the brightness within the beam's field of view as it moves through an arc of 1.2° . This is small compared to a beamwidth and beam smearing is thus negligible. Figure 20 shows only the nadir footprints obtained during a nominal MWR pass (see below), which are obtained once with each 30-s spin of the spacecraft. The half-power contour of each nadir beam footprint is depicted for both the 12° and 20° degree beamwidth antennas.

Although useful data are taken from pole to pole, the prime data for atmospheric sounding are obtained within the general latitude range $\pm 50^\circ$ where the beam footprints are small enough to resolve significant spatial features. The passage across this span takes about 40 minutes to complete and includes over 80 spacecraft rotations, during which nearly 10000 brightness temperature measurements are obtained on Jupiter with emission angles less than 50° . This range will also include the primary data obtained on the synchrotron emission beyond Jupiter's limbs. Outside of this range the MWR will accumulate data at lower resolution on Jupiter in the polar regions. This in turn is followed by an extended period up to several hours, where it will obtain data on the sky where the synchrotron emission is negligible for the purpose of establishing a low-temperature reference for the measurements obtained during perijove. The sky reference values used are based on maps obtained during cruise (Sect. 6.1.1).

The operational plan for the MWR has evolved since launch. Originally the radio science gravity experiment and the MWR atmospheric sounding experiments were assigned separate orbits since they were deemed to have incompatible observing and operational requirements; namely, to obtain optimal data the MWR preference is to scan along track though nadir, while the radio science experiment needs to point the high-gain antenna towards the Earth. In addition, it was anticipated that there would not be sufficient spacecraft power to operate both the MWR and Radio science experiments simultaneously. Hence in the original 14-day orbit design for the Juno mission, several early orbits (3, and 5 through 8) were planned as "MWR" orbits with nadir viewing obtained by orienting the spacecraft spin plane to

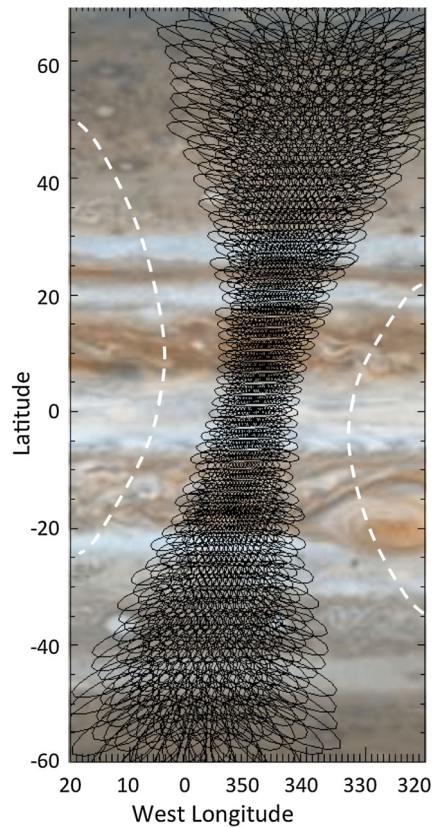
Fig. 20 MWR beam footprints during the predicted perijove pass of Orbit 6. Shown are the nadir half-power footprint tracks for the 20° beam of antenna A1 (*right track*) and the 12° beam footprint track of antenna A5 (*left track*) at the time each beam passes through nadir. Each footprint indicates one rotation of the spacecraft as it moves from north to south through the pass. The footprints drift westward as Jupiter rotates during the pass. Both tracks are in fact coaligned but are shown here with a 10° offset in longitude for illustration. The longitude shown on Jupiter is arbitrary and intended to show the range of atmospheric features that are resolved



contain Jupiter's center, while the rest were allocated as "Gravity" orbits with the MWR turned off. After launch, experience showed that these requirements were at least partially compatible and some compromise was possible. The spacecraft power limitation that drove the original decision was found to be conservative, and in addition it was argued that useful if not ideal MWR data could be obtained by operating during Gravity orbits. Finally, a case was made for a special MWR "Tilt" orbit that compensated for the longitudinal drift of MWR footprints due to Jupiter's rotation, as discussed below. The renegotiated baseline mission now consists of three orbit types, MWR, MWR Tilt, and Gravity orbits. In addition, the decision has been made to allow the MWR to remain on following the orbit insertion, and specifically through the first and second periapsis passes. The following then assumes the plan prior to Jupiter Orbit Insertion (JOI), which consists of a series of 14-day orbits following a Period Reduction Maneuver (PRM) occurring during the 2nd perijove pass on October 18, 2016. If the plan changes, it is expected that the same orbit options described below will still be possible although the dates and frequency of the perijove passes may be different.

Perijove Passes 1 and 2 (August 27 and October 18, 2016) Perijove pass 1 is the first close pass of Jupiter after orbit insertion, and occurs between the first and second 53-day capture orbits following JOI. For all practical purposes this is a Gravity orbit in that the high gain antenna remains pointed at the Earth, although the minimum angle to nadir during the pass is less than 4° . In all, the observing geometry is close to ideal for atmospheric measurements.

Fig. 21 Radiometer footprints (12° beamwidth) on Jupiter obtained by cross-track scanning during perijove 2 (every other footprint of every other scan shown, limited to 65° emission angle). The location of the Great Red Spot is shown as currently predicted



Perijove pass 2 occurs during the PRM where the orbit period is reduced to 14 days. Because the spacecraft is reoriented to fire the main engine in the velocity direction, this offers a unique geometry in which the scanning is perpendicular to the subspacecraft track on Jupiter rather than along it. This will allow an extended three-dimensional sounding of the atmospheric brightness in which longitudinal structure as well as latitudinal structure will be observed with depth. Figure 21 shows a swath of footprints that will be measured during this pass.

MWR Orbits (3, 5, 6, and 7) In these nominal MWR orbits the spin vector of the spacecraft is oriented perpendicular to the orbit plane so that the scan circle of the antenna beams always includes Jupiter nadir. Figure 22 depicts a sampling of the data obtained in a nominal MWR pass, showing sets of footprints obtained at each of five representative latitudes during a pass in which the emission angle varies from near nadir to 60° (50° at the extreme latitudes $\pm 50^\circ$). The footprints drift westward with time because of Jupiter's rotation, and grow in size away from nadir because of a combination of increasing range and slant angle projection. Varying footprint sizes and distributions introduce contributions to the limb-darkening measurements from horizontal atmospheric structure.

These contributions are anticipated to cause random errors in the determination of limb darkening that may exceed those due to instrument performance alone as given in Table 7. There are no atmospheric data on the spatial scales needed to estimate the magnitude of these observational effects, although they are likely in some cases to exceed the design limit

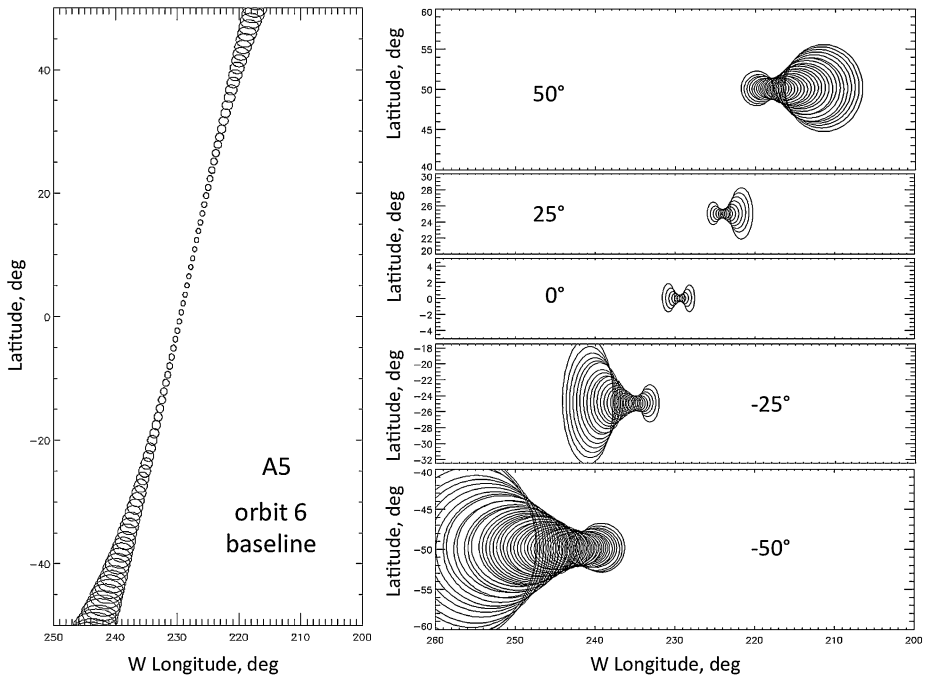


Fig. 22 Footprints at several latitudes are shown for all emission angles in the range $\pm 60^\circ$ ($\pm 50^\circ$ for latitudes $\pm 50^\circ$) for a regular MWR orbit. The footprints drift westward with time (or decreasing subspacecraft latitude) due to Jupiter's rotation

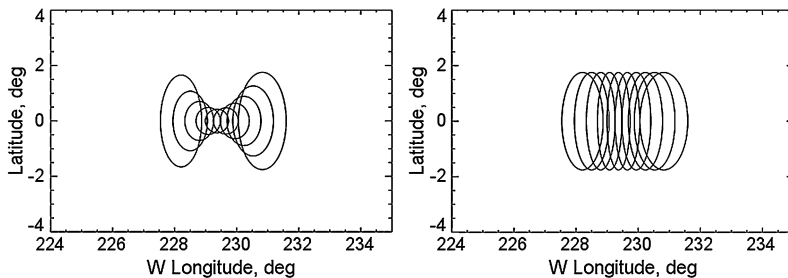


Fig. 23 Along-track averaging. *Left*: Footprints at 0° latitude; *Right*: Use of along-track averaging to produce effective footprints of equal dimension in latitude. The baseline MWR Orbit 6 is assumed

of 0.1% in the determination of the limb darkening parameter R . Such effects can be partially compensated by employing along-track averaging to minimize the contribution from latitudinal structure as shown in Fig. 23. The amount of averaging depends on the emission angle range one wishes to use for the determination of the limb darkening parameter and the desired spatial resolution. The impact of such structure will be studied after atmospheric structural data are obtained in Jupiter orbit. One possible benefit of uncompensated longitudinal drift in footprints at each latitude is that limited three-dimensional mapping (in latitude, longitude, and depth) may be possible.

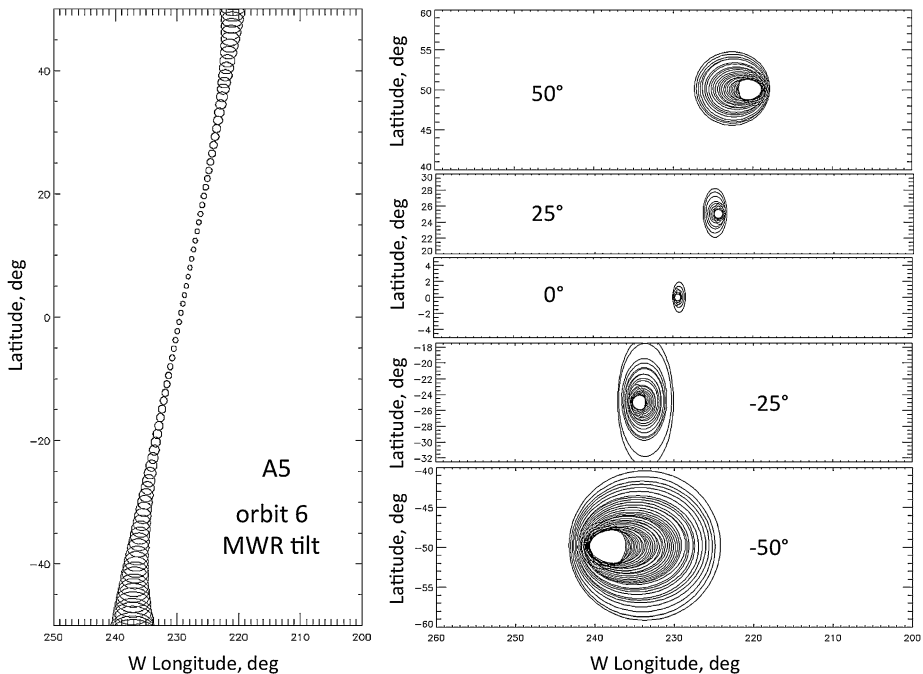


Fig. 24 Footprints for an MWR Tilt orbit in which a 14° tilt of the spacecraft orbit out of the ecliptic is assumed. The longitude drift due to Jupiter's rotation seen in Fig. 22 is largely compensated for by this tilt

MWR Tilt Orbits (8 and 14) The westward footprint drift incurred in nominal MWR orbits is effectively eliminated in MWR Tilt orbits, which provides another strategy for dealing with the effects of spatial structure on the determination of limb darkening. In these orbits the spacecraft spin vector is oriented approximately 14° out of the equatorial plane of Jupiter to provide a different orientation of the beam footprints with respect to the subspacecraft track. Figure 24 presents the same study as for the regular MWR orbit in Fig. 22, showing that this compensates (to a good approximation) for the longitudinal drift of the footprints. The nadir is now only viewed at a single latitude (the equator) in these orbits, however. This approach will allow us to minimize the contribution due to longitudinal structure in the determination of the limb-darkening parameter.

Gravity Orbits (All Remaining Orbits) The orientation in a Gravity orbit is not ideal for the measurement of the emission-angle dependence of the emission but allows useful data to be obtained that includes the possibility for longitudinal as well as latitudinal mapping. The nadir is never viewed, although the nadir offset is relatively small for orbits in the early half of the mission. The total number of atmospheric states observed is thus usefully enlarged, at little cost.

7 Data Analysis

The MWR data analysis task begins with the processing of the time-ordered raw data from the instrument and will ultimately extend to the achievement of the scientific objectives of

the MWR experiment. We discuss below the pipeline processing to deliver the calibrated antenna temperature measurements, followed by an outline of the approaches to subsequent analyses that address the ultimate objectives. The details of the latter are left to future papers.

7.1 Data Processing Pipeline

The first phase of the analysis is the conversion of raw data to calibrated antenna temperatures. The MWR pipeline is an automated process that receives the raw radiometric data and sampled engineering data downlinked from the spacecraft and processes it through the Juno Ground Data System to obtain a set of time-ordered calibrated radiometric antenna temperatures and associated engineering data at 100-ms intervals. The first step in the pipeline is to produce a set of time-ordered data at Level 2 (from CODMAC, Committee on Data Management, Archiving, and Computation) that consists of data records obtained in sequential 100-ms integrations. Each such record consists of time, raw radiometer counts, switch setting information, and engineering data (temperatures and voltages) converted to physical units.

From these we obtain the (CODMAC) Level-3 data in which the raw radiometric data for each 100-msec data record have been converted to calibrated radiances (antenna temperatures) in degrees Kelvin using the best current instrument model, and where the sparsely sampled engineering data have been interpolated to provide best-estimate values. Only those records that contain a radiance measurement through the antennas are retained, so that there are gaps in the Level 3 data, with those records usurped by a reference load or noise-diode firing for calibration missing (cf. Fig. 10). The sky brightness from the cruise maps is used as a reference source for the removal of slow offset drifts. The cold sky is observed before and after perijove as the antenna fields of view rotate away from Jupiter, but within the nearly two-hour passage centered on perijove the synchrotron emission is seen in all directions. Hence the sky reference must be obtained before and after perijove when the spacecraft is outside the belts, the times for which will vary with channel because of the strong frequency dependence of this emission. This leads to stability requirements on the receivers (as part of the ATC error budgeted in Table 2) in order to establish the baseline over time intervals up to two hours.

The Level 2 and Level 3 data are scheduled for delivery for archiving in the Atmospheres Node of the Planetary Data System. Only the Level-3 data may be considered useful for subsequent data analysis, however. While the Level-2 data are unchanged unless delayed records are added, the Level-3 data will be periodically revised as new calibration data are obtained or calibration models improved.

7.2 Subsequent Analysis and Interpretation

There are two paths for the data analysis. First, we may apply the antenna pattern correction (APC) described in Sect. 5.2.1 to transform the measured antenna temperatures into the equivalent of a Gaussian convolution of the actual brightness temperatures (plus noise and residual instrumental effects), which in many cases are readily deconvolved to obtain brightness temperatures. This takes the instrument out of the way and provides brightness temperatures with which to directly address the ultimate objectives. A second approach is to use our knowledge of the instrument along with models of the sources (Jupiter and the synchrotron belts) to synthesize the measured antenna temperatures. We have developed an “Instrument Simulator” that uses the reconstructed geometry of the spacecraft trajectory and orientation to model the observations directly as antenna temperatures. The models

may then be iterated parametrically to match the synthesized data with the actual measurements in order to determine their unknown properties, bypassing the deconvolution to obtain brightness temperatures. An essential element of either approach is our ability to compute accurate brightness temperatures for given models of Jupiter's atmosphere and the radiation belts, where by "accurate" in this context we mean calculated brightness temperatures with a fidelity commensurable with the instrumental measurement capabilities. These are limited only by the uncertainties given by the validated instrument error breakdown in Table 7, and by the residual uncertainties in the JAMRT absorption coefficients.

7.3 Prospects for Jupiter

7.3.1 Radiation Belts

Our two *a priori* synchrotron models can each feed predicted maps into the simulator to produce a predicted synchrotron contribution for every individual measurement by the MWR. For the initial data analysis to remove synchrotron emission from the atmospheric measurements, we can simply scale these predictions by the direct observation of synchrotron emission within each spin, relying on the large gain ratio between the main antenna beam and back lobes to reduce any error due to imperfections in the model. As the orbital mission progresses, the less complex synchrotron model (Adumitroaie et al. 2016) will be adjusted to more accurately match the MWR observations. Ultimately, the physics-based model for the synchrotron emission by Santos-Costa and Bolton (2009) will be combined with the magnetic field map produced by the Juno Magnetic Field Investigation to produce a detailed description of Jupiter's radiation belts.

7.3.2 Jupiter Atmosphere

Juno will obtain up to 36 slices of the atmosphere in latitude that will show brightness temperature variations caused by spatial variations in atmospheric composition, temperature, and cloud opacity to depths as great as several hundred bars. Because almost all atmospheric data obtained prior to Juno refer to the vicinity of the ammonia cloud region, the Juno MWR data add a new dimension to address fundamental questions about the deep structure and dynamics of Jupiter's atmosphere. Observations of Jupiter with the VLA (de Pater et al. 2001, 2016) and current work using the Cassini microwave radiometer to map Saturn at 2.2-cm wavelength (Janssen et al. 2013) have demonstrated the capability of microwave remote sensing to determine the cloud-level distribution of ammonia, while the deep-level sounding at the MWR frequencies will extend this capability well below the level where water clouds form. How deep Jupiter's zones, belts, and other features penetrate is one of the outstanding questions in Jovian atmospheric dynamics. The patterns of ammonia and water distribution below the clouds are expected to correlate with dynamical features at cloud-top level, allowing us to examine the deep roots of features like the Great Red Spot, the belts and zones, and the 5- μm hot spots.

The distribution of water and ammonia below Jupiter's cloud-tops is a major unresolved issue, defying definitive determination by existing remote sensing data and only partially and locally measured by the Galileo atmospheric entry probe (Folkner et al. 1998; Sromovsky et al. 1998; Mahaffy et al. 1999). The expected vertical and horizontal resolution of these primary volatiles at sub-cloud levels by the Juno MWR will be key not only to the determination of their global abundances, but also to the diagnosis of the planet's deep circulation and meteorology. The sensitivities for the retrieval of global abundances of

deeply mixed ammonia and water vapor from MWR observations are readily computed if the basic structural parameters of the atmosphere are assumed. Let us assume a hydrostatic atmosphere and a simple model with uniformly mixed water and ammonia up to their respective saturation levels, above which the mixing ratios follow their saturation curves and the lapse rates follow their wet adiabats. The deep mixing ratios of water vapor and ammonia are then determined by fitting the computed radiances to simulated measurements of the limb darkening parameter R (Eq. (3)). This is the case shown in Fig. 4, for which we have estimated that with the nominal measurement uncertainties in Table 7 we can achieve retrievals of H_2O and NH_3 to precisions of about 30% and 2% respectively. The latter is in fact better than our knowledge of the ammonia absorption coefficient would allow, which would lead to a somewhat larger uncertainty (roughly 5%).

Jupiter's atmospheric structure is anticipated to be more complex than that of a moist adiabat. As the major source of microwave absorption in the Jovian atmosphere, ammonia and its distribution must be dealt with first. Earth-based mapping has established that ammonia is generally depleted in the atmosphere above the 6-bar level. Together with the Galileo probe results, observations to the present have been taken to show that ammonia is depleted within and somewhat below the ammonia cloud region around 0.5 bars (de Pater and Massie 1985; de Pater et al. 2001, 2016; Gibson et al. 2005). The cause for this remains an outstanding question. The Earth-based approach is inherently limited in the depths that can be probed, however, and fundamental questions remain as well about how deep this depletion extends, how it is distributed, and what the deep uniformly mixed abundance really is. Water vapor contributes less to the microwave absorption than ammonia but can play a major role in transport and condensation in the circulation balance owing to both its relatively large contribution to the mean molecular weight and its uniquely large enthalpy of vaporization. Water's signature in a dynamic atmosphere will be characterized by its ability to generate structure at levels where it condenses as well as by its effect on the adiabat. While this might be difficult for point measurements and global average properties, the MWR experiment will take advantage of the wide range of atmospheric examples presented by the pole-to-pole scans, which sample a wide variety of atmospheric states and offer a number of possible approaches to determining these deep mixing ratios. These possibilities have been studied for planning and software development purposes, but will not be fully known until we arrive at Jupiter.

8 Summary

Jupiter will be the first gas giant planet to be explored by a multi-wavelength microwave remote-sensing radiometer on board a spacecraft. The Juno MWR has been designed to provide the most complete and accurate set of microwave remote sensing data on Jupiter that is possible within the constraints of the Juno mission. It will sample the atmospheric thermal radiation at close range from depths extending from the ammonia cloud region at around the 0.7-bar pressure level to levels in excess of 1000 bars. The data it provides will address the primary scientific objectives of the MWR investigation: determination of the dynamical properties of Jupiter's subcloud atmosphere; and determination of the global abundance of oxygen present in the atmosphere as water deep below the visible cloud deck. The key to the experiment is the measurement of the emission-angle dependence of the thermal radiation at each frequency relative to atmospheric local normal, which can recover the information contained in the microwave spectrum without the need for extraordinary absolute calibrations of the microwave radiometers. The performance of the MWR in all six

channels determined in the years since launch shows that all design requirements have been met, and in some cases significantly exceeded, that will enable its promised performance on arrival at Jupiter in August 2016.

Acknowledgements The work described in this paper was conducted at the Jet Propulsion Laboratory (JPL), California Institute of Technology, under contract with the National Aeronautics and Space Administration (NASA). The author wishes to thank the numerous contributors from the Juno Project and the Lockheed-Martin spacecraft team, without whom this ambitious project would not have been possible.

References

- V. Adumitroaie, S.M. Levin, D. Santos-Costa, S. Gulkis, M.A. Janssen, in *Aerospace Conference 2016* (IEEE, New York, 2016), pp. 1–11
- K. Altwegg et al., *Science* **347**, 1261952 (2015)
- M. Asplund, N. Grevesse, J. Sauval, P. Scott, *Ann. Rev. Astron. Astrophys.* **47**, 481–522 (2009)
- S.K. Atreya, *Atmospheres and Ionospheres of the Outer Planets and Their Satellites* (Springer, New York, 1986)
- S.K. Atreya, M.H. Wong, T.C. Owen, P.R. Mahaffy, H.B. Niemann, I. de Pater, *Planet. Space Sci.* **47**, 1243–1262 (1999)
- S.K. Atreya, P.R. Mahaffy, H.B. Niemann, T.C. Owen, in *Highlights of Astronomy*, vol. 12, ed. by H. Rickman (Springer, New York, 2002), pp. 597–601
- S.K. Atreya, A. Crida, T. Guillot, J.I. Lunine, N. Madhusudhan, M. Mousis, in *Saturn in the 21st Century*, ed. by K. Baines, M. Flasar, N. Krupp, T. Stallard (Cambridge Univ. Press, Cambridge, 2017)
- J.W.M. Baars, R. Genzel, I.I.K. Pauliny-Toth, A. Witzel, *Astron. Astrophys.* **61**, 99–106 (1977)
- J.J. Barnes, D.A. Kring, R. Tartese, I.A. Franchi, M. Anand, S.S. Russell, *Nat. Commun.* **7**, 11684 (2016)
- A. Bellotti, P.G. Steffes, G. Chinsomboon, *Icarus* **280**, 255–267 (2016)
- G.L. Berge, S. Gulkis, in *Jupiter*, ed. by T. Gehrels (Univ. of Arizona Press, Tucson, 1976), pp. 621–692
- G.L. Bjoraker, M.H. Wong, I. de Pater, M. Ádámkóvics, *Astrophys. J.* (2015). doi:[10.1088/0004-637X/810/2/122](https://doi.org/10.1088/0004-637X/810/2/122), astro-ph.EP
- S.T. Brown, S. Desai, W. Lu, A. Tanner, *IEEE Trans. Geosci. Remote Sens.* **45**(7), 1908–1920 (2007). doi:[10.1109/TGRS.2006.888098](https://doi.org/10.1109/TGRS.2006.888098)
- S.T. Brown, *IEEE Trans. Geosci. Remote Sens.* **51**, 1531–1543 (2013)
- N.F. Chamberlain, J.C. Chen, R.E. Hodges, R.C. Hughes, J.K. Jakoboski, in *IEEE APS/URSI Conference*, Toronto, Canada (2010)
- J.E.P. Connerney, M. Bann, J.B. Bjarno, T. Denver, J. Espley, J.L. Jorgensen, P.S. Jorgensen, P. Lawton, A. Malinikova, J.M. Merayo, S. Murphy, J. Odom, R. Oliverson, R. Schurr, D. Sheppard, E.J. Smith, *Space Sci. Rev.* (2017). doi:[10.1007/s11214-017-0334-z](https://doi.org/10.1007/s11214-017-0334-z)
- I. de Pater, S.T. Massie, *Icarus* **62**, 143–171 (1985)
- I. de Pater, J.R. Dickel, *Astrophys. J.* **308**, 459–471 (1986)
- I. de Pater, D. Dunn, P. Romani, K. Zahnle, *Icarus* **149**, 66–78 (2001)
- I. de Pater, D. DeBoer, M. Marley, R. Freedman, R. Young, *Icarus* **173**, 425–438 (2005)
- I. de Pater, R.J. Sault, B. Butler, D. DeBoer, M.H. Wong, *Science* **352**, 1198–1201 (2016)
- K. Devaraj, P.G. Steffes, D. Duong, *Icarus* **241**, 165–179 (2014)
- D.T. Duong, P.G. Steffes, S. Noorizadeh, *Icarus* **229**, 121–131 (2014)
- G.B. Field, *J. Geophys. Res.* **64**, 1169–1177 (1959)
- W.M. Folkner, R. Woo, S. Nandi, *J. Geophys. Res.* **103**(E10), 22,847–22,855 (1998)
- J. Gibson, W.J. Welch, I. de Pater, *Icarus* **173**, 439–446 (2005)
- H.B. Garrett, S.M. Levin, S.J. Bolton, R.W. Evans, B. Bhattacharya, *Geophys. Res. Lett.* **32**, 4104–4108 (2005)
- D. Gautier, F. Hersant, O. Mousis, J.I. Lunine, *Astrophys. J.* **550**, L227–L230 (2001)
- S. Gulkis, T.R. McDonough, H. Craft, *Icarus* **10**, 421–427 (1969)
- S. Gulkis, R. Poynter, *Phys. Earth Planet. Inter.* **6**, 36–43 (1972)
- T.R. Hanley, P.G. Steffes, B.M. Karpowicz, *Icarus* **202**, 316–335 (2009)
- J. Harrington, I. de Pater, S.H. Brecht, D. Deming, V. Meadows, K. Zahnle, P.D. Nicholson, in *Jupiter. The Planet, Satellites and Magnetosphere*, ed. by F. Bagenal, T.E. Dowling, W.B. McKinnon (Cambridge Univ. Press, Cambridge, 2004), p. 159–184
- M. Heimpel, T. Gastine, J. Wicht, *Nat. Geosci.* **9**, 19–23 (2016)
- F. Hersant, D. Gautier, J.I. Lunine, *Planet. Space Sci.* **52**, 623–641 (2004)

- M.A. Janssen, *Atmospheric Remote Sensing by Microwave Radiometry* (Wiley, New York, 1993)
- M.A. Janssen, C.S. Ruf, S.J. Keihm, *IEEE Trans. Geosci. Remote Sens.* **33**, 138–146 (1995)
- M.A. Janssen, M.D. Hofstadter, S. Gulkis, A.P. Ingersoll, M. Allison, S.J. Bolton, L.W. Kamp, *Icarus* **173**, 447–453 (2005)
- M.A. Janssen, A. Ingersoll, M.D. Allison, S. Gulkis, A. Laraia, K. Baines, S. Edgington, Y. Anderson, K. Kelleher, *Icarus* **226**, 522–535 (2013)
- B.M. Karpowicz, P.G. Steffes, *Icarus* **212**, 210–223 (2011a)
- B.M. Karpowicz, P.G. Steffes, *Icarus* **214**, 783 (2011b)
- K.I. Kellerman, *Astron. Astrophys.* **500**, 143–144 (2009)
- S.M. Levin, S. Bolton, B. Bhattacharya, S. Gulkis, M. Klein, R. Thorne, *Geophys. Res. Lett.* **28**, 903–906 (2001)
- Y. Lian, A.P. Showman, *Icarus* **207**, 373–393 (2010)
- G.F. Lindal, G.E. Wood, G.S. Levy, J.D. Anderson, D.N. Sweetnam, H.B. Hotz, B.J. Buckles, D.P. Holmes, P.E. Doms, V.R. Eshleman, G.L. Tyler, T.A. Croft, *J. Geophys. Res.* **86**, 8721 (1981)
- C.H. Lineweaver, L. Tenario, G.F. Smoot, P. Keegstra, A.J. Banday, P. Lubin, *Astrophys. J.* **470**, 38–42 (1996)
- J. Liu, T. Schneider, *J. Atmos. Sci.* **67**, 3652–3672 (2010)
- J.J. Liu, T. Schneider, *J. Atmos. Sci.* **72**, 389–408 (2015)
- E. Lorenz, *Tellus* **7**, 157–167 (1955)
- J.I. Lunine, D.J. Stevenson, *Astrophys. J. Suppl. Ser.* **58**, 493–531 (1985)
- V. Lucarini, S. Pascale, R. Boschi, E. Kirk, N. Iro, *Astron. Nachr.* **334**, 576–588 (2013)
- P.R. Mahaffy, H.B. Niemann, J.E. Demick, *Bull. Am. Astron. Soc.* **31**, 5205 (1999)
- P.R. Mahaffy, H.B. Niemann, A. Alpert, S.K. Atreya, J. Demick, T.M. Donahue, D.N. Harpold, T.C. Owen, *J. Geophys. Res., Planets* **105**(E6), 15061–15071 (2000)
- B. Marty, *Earth Planet. Sci. Lett.* **313**, 56–66 (2012)
- E.C. Morris, R.W. Parsons, *Aust. J. Phys.* **23**, 335–349 (1970)
- H.B. Niemann, S.K. Atreya, G.R. Carignan, T.M. Donahue, J.A. Haberman, D.N. Harpold, R.E. Hartle, D.M. Hunten, W.T. Kasprzak, P.R. Mahaffy, T.C. Owen, N.W. Spencer, S.H. Way, *Science* **272**, 846–849 (1996)
- H.B. Niemann et al., *J. Geophys. Res., Planets* **103**, 22831–22845 (1998)
- T. Owen, A. Barnun, I. Kleinfeld, *Nature* **358**, 43–46 (1992)
- T. Owen, A. Barnun, *Icarus* **116**, 215–226 (1995)
- T.C. Owen, P.R. Mahaffy, H.B. Niemann, S.K. Atreya, T.M. Donahue, A. Bar-Nun, I. de Pater, *Nature* **402**, 269–270 (1999)
- B.M. Partridge, B.M. Lopez-Caniego, R.A. Perley, J. Stevens, B.J. Butler, G. Rocha, B. Waler, A. Zacchei, [arXiv:1506.02892](https://arxiv.org/abs/1506.02892) [astro-ph.CO] (2016)
- J.P. Peixoto, A.H. Oort, *Physics of Climate* (Am. Inst. of Physics, New York, 1992)
- J. Peng, C.S. Ruf, S.T. Brown, J. Piepmeier, in *IEEE International Geoscience and Remote Sensing Symposium*, Barcelona (2007), pp. 2416–2418
- R.A. Perley, B.J. Butler, *Astrophys. J. Suppl. Ser.* **204**, 1–20 (2013)
- J.B. Pollack, O. Hubickyj, P. Bodenheimer, J. Lissauer, M. Podolak, Y. Greenzweig, *Icarus* **124**, 62–85 (1996)
- D. Santos-Costa, S.J. Bolton, *Planet. Space Sci.* **56**, 326–345 (2009)
- D. Santos-Costa, I. de Pater, R.J. Sault, M.A. Janssen, S.M. Levin, S.J. Bolton, *Astron. Astrophys.* **568**(A61), 1–11 (2014)
- R.J. Sault, C. Engel, I. de Pater, *Icarus* **168**, 336–343 (2004)
- G. Schubert, J. Mitchell, in *Comparative Climatology of Terrestrial Planets*, ed. by S.J. Mackwell, A.A. Simon-Miller, J.W. Harder, M.A. Bullock (Univ. of Arizona Press, Tuscon, 2013), pp. 181–191
- A. Seiff, D.B. Kirk, T.C.D. Knight, R.E. Young, J.D. Mihalov, L.A. Young, F.S. Milos, G. Schubert, R.C. Blanchard, D. Atkinson, *J. Geophys. Res.* **103**, 22857 (1998)
- A.P. Showman, I. de Pater, *Icarus* **174**, 192–204 (2005)
- S.S. Sobjaerg, N. Skou, J.E. Balling, *IEEE Trans. Geosci. Remote Sens.* **47**(9), 3134–3139 (2009)
- P.G. Steffes, T.R. Hanley, B.M. Karpowicz, K. Devaraj, S. Noorizadeh, D. Duong, G. Chinsomboon, A. Bellotti, M.A. Janssen, S.J. Bolton, *Space Sci. Rev.* (2017). doi:[10.1007/s11214-016-0265-0](https://doi.org/10.1007/s11214-016-0265-0)
- L.A. Sromovsky, A.D. Collard, P.M. Fry, G.S. Orton, M.T. Lemmon, M.G. Tomasko, R.S. Freedman, *J. Geophys. Res.* **103**, 22929–22978 (1998)
- K. Sugiyama, K. Nakajima, M. Odaka, K. Kuramoto, Y.Y. Hayashi, *Icarus* **229**, 71–91 (2014)
- F. Tabataba-Vakili, P.L. Read, S.R. Lewis, L. Montabone, T. Ruan, Y. Wang, A. Valeanu, R. Young, *Geophys. Res. Lett.* **42**, 8320–8327 (2015)

- S.I. Thomson, M.E. McIntyre, *J. Atmos. Sci.* **73**, 1119–1141 (2016)
A.R. Vasavada, A.P. Showman, *Rep. Prog. Phys.* **68**, 1935–1996 (2005)
F. Wentz, D. Levine, Remote sensing systems. Technical report 011811 (2011)
M.H. Weatherspoon, L.P. Dunleavy, *IEEE Trans. Microw. Theory Tech.* **54**(2), 608–614 (2006)
M.H. Wong, P.R. Mahaffy, S.K. Atreya, H.B. Niemann, T.C. Owen, *Icarus* **171**, 153–170 (2004)
G.T. Wrixon, W.J. Welch, D. Thornton, *Astrophys. J.* **169**, 171–183 (1971)